

The Pennsylvania State University

The Graduate School

Department of Meteorology

SEA-SURFACE STRESS VARIABILITY
IN THE BOUNDARY LAYER

A Thesis in
Meteorology

by

Bruce Allen Lambert, Jr.

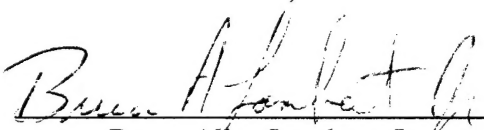
Submitted in Partial Fulfillment
of the Requirements
for the Degree of

Master of Science

August 1995

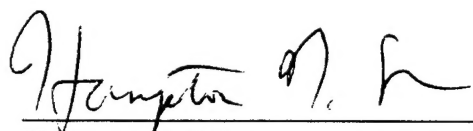
Accession For	
NTIS CRA&I	<input checked="checked" type="checkbox"/>
DTIC TAB	<input type="checkbox"/>
Unannounced	<input type="checkbox"/>
Justification	
By	
Distribution /	
Availability Codes	
Dist	Avail and/or Special
A-1	

I grant The Pennsylvania State University the nonexclusive right to use this work for the University's own purposes and to make single copies of the work available to the public on a not-for-profit basis if copies are not otherwise available.


Bruce Allen Lambert, Jr.

We approve the thesis of Bruce Allen Lambert, Jr.

Date of Signature



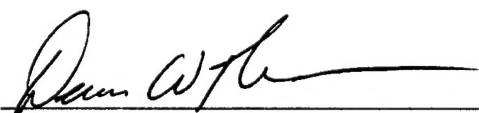
Hampton N. Shirer
Associate Professor of Meteorology
Thesis Adviser

21 July 95



Robert Wells
Professor of Mathematics

21 July 95



Dennis W. Thomson
Professor of Meteorology
Head of the Department of Meteorology

21.7.95

ABSTRACT

There is great potential for the use of satellite- or aircraft-borne synthetic aperture radar (SAR) imagery for analysis of meteorological systems. However, the interpretation of SAR imagery requires increased understanding of processes that change the state of the sea surface. Wind stress that results from kilometer-scale boundary layer spanning eddies (BLSE) produces sea-surface stress patterns responsible for some of this sea-surface variability. In this study, a Galerkin model of these BLSE, which take the form of two-dimensional rolls or three-dimensional convective cells, is modified with new boundary conditions to study their effect on sea-surface stress.

Previous investigations using spectral models have for simplicity been formulated using lower boundary conditions in which the stress and heat flux vanish. However these boundary conditions do not allow the study of stress variability at the sea surface. The marine atmospheric boundary layer model used here allows subgrid-scale heat and momentum fluxes at the lower boundary and has been shown in a previous study to capture much of the qualitative behavior of BLSE circulations. However, the model solution in this study had a maximum vertical velocity at the lower boundary that prevented the fluxes from being physically correct, and the solution did not equilibrate owing to an unknown energy source. The goal of this thesis is to investigate hypotheses concerning how these problems can be solved. These hypotheses are derived from an energetics analysis of the model equations that leads to the introduction of new lower boundary conditions to control the boundary energy terms. The model is then applied in a case study using Hi-Res 2 data as initial conditions to determine the velocity fields at the lower boundary that produce kilometer-scale sea-surface stress variability and to compare this pattern with that found on an ERS-1 SAR image.

The case study results demonstrate that the model with the new boundary conditions does indeed capture the spatial organization of BSLE and correctly reproduces an expected three-dimensional circulation. A linear analysis using a small-shear, light-wind profile and a -2°C air-sea temperature difference produces preferred aspect ratios whose magnitudes agree well with those derived from the SAR image. When these parameter values are input into the model, a quickly equilibrating solution, with total energy that is fairly constant, is obtained as expected from earlier studies. Also as expected, the wind profile and temperature profile modification coefficients become steady, while the BLSE circulation and temperature coefficients have a period matching that given by the linear analysis. Cross-sectional contours of the streamfunctions in the across-wind and along-wind directions show that the circulation fills the domain, with wavenumber one dominant, but with evidence that other wavenumbers contribute as well. The cross-sectional results also show that the temperature perturbation has a dominant wavenumber two pattern, with a maximum at the lower boundary where the thermal forcing is introduced. These streamfunction and temperature contours have patterns very similar to those given by much higher-resolution large-eddy simulation.

The most important result of the case study concerns the BLSE-induced sea-surface stress pattern. At the lower boundary, this pattern is obtained from the vector sum of the model-calculated winds and the background mean wind, all expressed relative to the ocean current. Via the standard drag law parameterization, the total horizontal wind speed is proportional to the square-root of the sea-surface stress magnitude. Quite pleasingly, the stress pattern on this planview matches the orientation and spacing of the stress pattern found on the SAR image. This result shows that the model is now ready to be used in further studies of how BLSE affect the sea-surface stress variability in different boundary layer configurations.

TABLE OF CONTENTS

LIST OF FIGURES.....	vi
LIST OF TABLES	viii
ACKNOWLEDGMENTS	ix
Chapter 1. INTRODUCTION.....	1
Chapter 2. MODEL DESCRIPTION AND MODIFICATIONS	5
2.1. Model Description	5
2.1.1. The Partial Differential Equations	8
2.1.2. The Spectral System.....	12
2.2. Energetics Analysis.....	15
2.3. Incorporation of New Boundary Conditions.....	21
2.4. The Computer Model.....	23
Chapter 3. HI-RES CASE STUDY.....	26
3.1. Description of Hi-Res 2 Data.....	27
3.2. Case Study Data and Preferred Parameter Values	28
3.3. BLSE Patterns	43
3.4. Case Study Conclusions.....	60
REFERENCES	61
Appendix A. MODEL ENERGETICS.	64
Appendix B. MODIFICATION OF THE VERTICAL BASIS FUNCTIONS	72
B.1. Vertical Basis Function Reformulation.....	72
B.2. Modification of Existing Program to Incorporate New Basis Functions.....	76

LIST OF FIGURES

2.1	A schematic cross-section of the marine atmospheric boundary layer, in which the surface layer is greatly exaggerated.....	6
3.1	Range of values of s_m and s_r for 17 June 1993 calculated from R/V Columbus Iselin observations.	31
3.2	Woodcock diagram (1975) determines circulation regimes from relative wind speed and air/sea temperature difference	32
3.3	Schematic plot of Re versus one aspect ratio while the other aspect ratio is fixed and $Ra = -1$	36
3.4	Contour plot of the real part of the last eigenvalue from the linear eigensystem analysis for $Re = 250$	38
3.5	Mean current-relative wind profile with predominantly speed shear that is used in case study.....	40
3.6	The square root of the sum of the squares for the 50 time-dependent amplitude coefficients.....	41
3.7	Time series of one of the time-dependent temperature amplitude coefficients (T_{11}), demonstrating that the bifurcating solution has periods of approximately 36 minutes and 9 minutes.	44
3.8	Domain cross-section of contoured streamfunctions: (a) $\tilde{\psi}^*$ and (b) $\tilde{\eta}^*$ in the cross-mean-wind direction \tilde{y}^* -across.	47
3.9	Domain cross-section of contoured streamfunctions: (a) $\tilde{\psi}^*$ and (b) $\tilde{\eta}^*$ in the along-mean-wind direction \tilde{x}^* -along.....	48
3.10	Domain cross-section of contoured temperature : (a) across-mean-wind direction \tilde{y}^* -across and (b) along-mean-wind direction \tilde{x}^* -along.	49
3.11	Domain cross-section of velocity vectors: (a) (\tilde{v}^*, w^*) and (b) (\tilde{u}^*, w^*) in the cross-mean-wind direction \tilde{y}^* -across.	50

3.12	Domain cross-section of velocity vectors: (a) (\tilde{v}^*, w^*) and (b) (\tilde{u}^*, w^*) in the along-mean-wind direction \tilde{x}^* -along.....	52
3.13	Dimensional vertical velocity profile for the center of an updraft.....	53
3.14	Vertical profile of the dimensional wind modification velocity components given by η_{0q}	54
3.15	Vertical profile of the dimensional wind modification velocity components given by ψ_{0q}	55
3.16	Vertical profile of the dimensionless temperature modification given by T_{0q}	57
3.17	Planview of complete horizontal dimensionless velocity field at the lower boundary $z^* = 0$	58
3.18	Planview of stress magnitudes at the lower boundary $z^* = 0$	59
B.1	Velocity vertical basis function (vertical velocity) profiles (B.7) - (B.9) for the three new wavenumbers.....	75

LIST OF TABLES

3.1	Hi-Res 2 observed MABL data.....	29
3.2	Parameter values used in case study.	34

ACKNOWLEDGMENTS

The research presented in this thesis was sponsored by the Office of Naval Research through grant N00014-90-J-4012. The financial support for my academic program was provided by the Air Force Institute of Technology (AFIT) Civilian Institution Program.

There are many people I want to thank for making this a successful project. Capt Louis Zuccarello did most of the work in deriving and writing the computer model. The computer model was excellently written and organized and he helped me through the initial stages of learning about this project and the model. Ms. Julie L. Schramm did much of the background work needed to implement this model. She developed the boundary conditions Zuccarello used and provided computer programs that allowed us to incorporate the boundary conditions into the model. The subroutine supplied by Dr. George S. Young, which was implemented by Mr. Dave V. Ledvina based on work done by Dr. Chris W. Fairall, was crucial to Julie's development of the boundary conditions. Dr. Young and Mr. Todd Sikora also played an important role in interpreting our results and offering many useful suggestions for further research. Mr. Edward Mansouri, Dr. Mark J. Laufersweiler, and Dr. Harry W. Henderson provided valuable computer and meteorological expertise. Dr. Jim Edson allowed us to use his data from Hi-Res 2. I also thank my AFIT colleagues for their help and camaraderie.

I want to especially thank Dr. Hampton N. Shirer and Dr. Robert Wells. They are the two individuals who really made the miraculous completion of this work possible. They both gave selflessly of their time and always answered my many questions. Dr. Wells provided the mathematical insight that was crucial to the further development of this model. I thank him for his support and encouragement. Dr. Shirer, thesis adviser,

gave me the opportunity to work on this project. He has proved to be an outstanding adviser, teacher, and friend. Dr. Shirer's professionalism and meteorological expertise have made working with him a real honor. I thank him for his tireless efforts and hope to work with both of them again.

Finally, I wish to give special thanks to my family. Deb has constantly given me a tremendous amount of support and love. I cannot thank her enough for being such a wonderful wife and a patient mother, while I have been busy with school work. My two daughters, MaryGrace and Katharine, have given me love and encouragement while we have been at Penn State. They have been understanding when Daddy had to work and could not play or read. The times we had as a family here have been very special and I feel that we are closer. My family's love and support have made the completion of my M.S. degree very rewarding.

Chapter 1

INTRODUCTION

There is great potential for the use of satellite- and aircraft-borne synthetic aperture radar (SAR) as meteorological and oceanographic observation systems (Vesecky and Stewart 1982). The variability of stress on the sea surface produces distinct patterns in SAR imagery. Secondary circulations within the marine atmospheric boundary layer (MABL) can modulate the sea-surface wave field and so can produce these discernible signatures. Evidence for these secondary circulations has been found by Thompson *et al.* (1983), Gerling (1986), and Alpers and Brümmer (1994), who studied the SAR signatures produced by roll circulations in the MABL. By correctly interpreting the signatures in the imagery, we can infer the atmospheric conditions in the ocean surface layer that lead to alternating regions of converging and diverging air at the surface (Gerling 1986; Alpers and Brümmer 1994). Thompson *et al.* (1983) noted that we must understand these effects theoretically before employing SAR as remote sensors of ocean surface winds. We model these circulations and use the model to study their effects on the sea-surface stress patterns through atmospheric modeling of the MABL flow.

Quasi-linear and cellular patterns, with spacing on the order of a kilometer, are commonly observed in SAR imagery (e.g., Visecky and Stewart 1982). There are two types of kilometer-scale circulations that affect sea-surface stress – roll circulations and convective cells. The first type is a quasi-two-dimensional feature, while the second type is a fully three-dimensional flow that may form independently of the rolls in less windy conditions (Woodcock 1940,1975; Deardorff, 1976). Etling and Brown (1993) have reviewed three fundamentally different mechanisms for the formation of rolls and cells in the boundary layer. The first two, the inflection point and parallel instabilities, are related

to the background wind shear. For the first mechanism there must be an inflection point in the wind profile and for the second, the time scale must be long enough that the Coriolis force becomes important. The third mechanism is thermal instability in which the driving force is an air/sea temperature difference. This thermal mode produces convection very much like Rayleigh-Bénard convection observed in the laboratory. Following Sikora and Young (1993), we call these rolls and cells boundary layer spanning eddies (BLSE). The BLSE vertical scale is the boundary layer depth, and they transfer momentum and heat down to the top of the surface layer. From there, small scale eddies are responsible for the final transfer of momentum and heat to the sea surface.

A number of people have studied BLSE and have modeled them using nonlinear dynamical systems (e.g., Shirer 1986; Laufersweiler and Shirer 1989, 1995; Haack and Shirer 1992). These studies have sought to identify the dominant forcing mechanisms and characteristic spatial and temporal responses of these boundary layer circulations as the forcing rate varies. These nonlinear, Galerkin models, which are based on the Boussinesq system of equations and use sinusoidal basis functions, provide wind profile modifications, preferred orientation angles and wavelengths, and economy in the study of bifurcation and stability properties. These models also yield profiles of the vertical fluxes of horizontal momentum and heat. For simplicity, the lower boundary conditions used in these models are rigid and stress-free. Since we are studying the effects of these BLSE on stressing the sea surface, these boundary conditions are not appropriate for this study. We need a model that allows the heat and momentum fluxes pass through the surface layer and penetrate the lower boundary.

Zuccarello (1994) has developed a nonlinear, Boussinesq, three-dimensional boundary layer model that allows nonzero subgrid-scale heat and momentum fluxes at the lower boundary. He uses similarity theory to specify the boundary conditions. The

bottom of the domain is set at 10 *m* above the sea surface, where the lower boundary conditions are chosen to represent wind and temperature values typically observed at this height in the surface layer. Application of the stability-modified similarity relationships leads to constant forcing parameters that are used in the specification of the lower boundary conditions. These boundary conditions allow for a more realistic incorporation of thermal forcing, which in earlier models (e.g., Haack and Shirer, 1992) is spread throughout the entire vertical domain and represented by the Rayleigh number *Ra*. In reality, the thermal forcing at the lower boundary should drive the system and the value of the traditional Rayleigh number should be inferred from the model solutions. Finally, and for simplicity, the upper boundary conditions are rigid, stress-free, and perfectly conducting as in the earlier models.

The vertical basis functions for the model expansions are found by solving a more realistic eigenfunction problem based on the new boundary conditions (Zuccarello, 1994). These basis functions are expressed in terms of exponential and trigonometric functions. The horizontal basis functions are composed of trigonometric functions and are cyclic. The spectral model, derived from the Boussinesq system using these expansions, is incorporated into the FORTRAN program that does the numerical integration of the model and subsequent simulation of the BLSE circulations.

Zuccarello (1994) got fairly good results in a simple case study. The case study results show the model properly captures the spatial organization of the roll circulations. The results also revealed that the temporal periodicity of the system is consistent with both physical and numerical analyses of the solution based purely on advection by the cross-roll mean wind. The system of equations and many of the physical assumptions made are appropriate for modeling BLSE in a marine environment. However, Zuccarello discovered several problems during his case study. The first problem is an unknown

energy source that prevents the model from equilibrating during integration. The second problem is with the vertical velocity. In the updrafts, the maximum vertical velocity is at the lower boundary. This forces the maximum momentum fluxes to be in the lowest 200 *m* of the boundary layer, instead of in the middle of the boundary as typically observed.

The focus of this study is to continue Zuccarello's (1994) work in studying the effects of the BLSE on sea surface stress variability. We begin with an energetic analysis of the original system of equations and the model equations to locate and identify how to control the energy sources and sinks. The analysis reveals a large number of energy boundary terms in the model. The addition of some new boundary conditions eliminates most of these boundary terms and controls the vertical velocity at the lower boundary. In Chapter 2 we review the model, describe the energetic analysis, and discuss changes we make in the model. In Chapter 3, we look at some case studies based on observational data from the second High Resolution Remote Sensing Experiment (Hi-Res). In Chapter 4, we conclude by reviewing the improvements in the model and the case study results, and we look at future areas to study with this model.

Chapter 2

MODEL DESCRIPTION AND MODIFICATIONS

We use a spectral model developed by Zuccarello (1994) to study boundary layer spanning eddies (BLSE). Zuccarello finds the model accurately captures the spatial organization of roll circulations and the temporal periodicity of the system, as given by advection by the constant cross-roll mean wind component. However, the model also has some problems, and Zuccarello suggests that an energetics analysis be performed to find the unknown energy source preventing the model from equilibrating during integration. He also recommends an examination of the boundary conditions to determine why the vertical velocity is too large at the lower boundary.

We extend the work done by Zuccarello by examining the model development and performing a diagnostic energy analysis to identify all the energy sources and sinks in the system. Our results indicate a number of boundary terms as possible, unrealistic energy sources or sinks. However, the analysis also indicates that introduction of additional boundary conditions will eliminate all of these unrealistic boundary terms. We then modify the model to include these boundary conditions and so better control the system energy.

2.1. Model Description

The model description that follows is a summary of the model development chapter of Zuccarello (1994). For a complete description of the model development, we direct the reader to Zuccarello (1994).

The convective nature of boundary layer roll circulations allows the use of a model based on the shallow Boussinesq system. This model represents roll circulations by perturbations superimposed on a basic state that is time-independent, isopycnic, hydrostatic, and horizontally moving (Shirer 1986). We assume that the perturbations possess a three-dimensional structure, and so we consider both mean-wind-perpendicular and mean-wind-parallel variations. The horizontal domain is infinite and cyclically continuous, and bounded by the planes $x = 0, y = 0$ and $x = L_x, y = L_y$, where L_x and L_y are the domain wavelength components. If the domain contained a single diagonal roll, then it would have wavelength $L = (1/L_x^2 + 1/L_y^2)^{1/2}$. The vertical domain ranges from $z = h_{LB}$ to $z = z_T$, where h_{LB} is the height of the lower boundary and z_T is the cloud top height or inversion base (Fig. 2.1). Only the part of the circulation above h_{LB} is specifically modeled; the part below h_{LB} is parameterized via boundary conditions based surface layer similarity theory. In dimensionless form the domain is defined by $0 \leq x^* \leq 1$, $0 \leq y^* \leq 1$, and $0 \leq z^* \leq 1$.

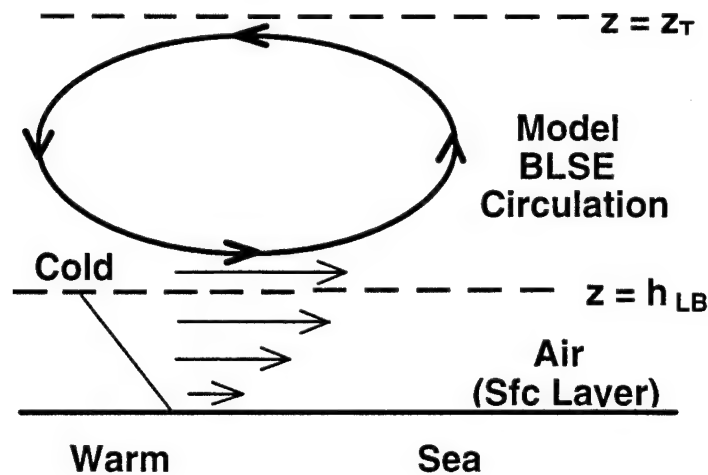


Fig. 2.1. A schematic cross-section of the marine atmospheric boundary layer, in which the surface layer is greatly exaggerated. In the surface layer the temperature decreases and the wind increases with height.

The basic state, known as the conductive state and denoted by subscript 0, is given by

$$\mathbf{v}_0(z) = \mathbf{V}(z) = U(z)\mathbf{i} + V(z)\mathbf{j} \quad (2.1)$$

$$\rho_0 = \rho_{00} \quad (2.2)$$

$$T_0(z) = T_{00} - \Delta_z T(z/z_T) \quad (2.3)$$

$$p_0(z) = p_{00} - \rho_{00}gz, \quad (2.4)$$

where subscript 00 denotes the value at the sea surface, $U(z)$ and $V(z)$ are the components of the mean horizontal wind, and $\Delta_z T/z_T$ is a constant lapse rate given by the temperature difference $\Delta_z T$ between the inversion base and the sea surface. The three-dimensional secondary circulation, denoted by primes, is given by

$$u'(x, y, z, t) = u(x, y, z, t) - U(z) \quad (2.5)$$

$$v'(x, y, z, t) = v(x, y, z, t) - V(z) \quad (2.6)$$

$$w'(x, y, z, t) = w(x, y, z, t) \quad (2.7)$$

$$\rho'(x, y, z, t) = \rho(x, y, z, t) - \rho_{00} \quad (2.8)$$

$$T'(x, y, z, t) = T(x, y, z, t) - T_0(z) \quad (2.9)$$

$$p'(x, y, z, t) = p(x, y, z, t) - p_0(z). \quad (2.10)$$

In the Boussinesq system, compression is considered negligible. Other approximations include writing the equation of state in a normalized form and linearizing the pressure gradient force (Shirer 1987).

2.1.1. The Partial Differential Equations

The Boussinesq system of equations for the perturbation temperature T' and the perturbation velocity vector \mathbf{v}' takes the form (e.g., Shirer 1986)

$$\frac{\partial T'}{\partial t} + \mathbf{V} \cdot \nabla T' + \mathbf{v}' \cdot \nabla T' = \frac{\Delta_z T}{z_T} w' + \kappa \nabla^2 T' \quad (2.11)$$

$$\frac{\partial \mathbf{v}'}{\partial t} + \mathbf{V} \cdot \nabla \mathbf{v}' + w' \frac{\partial \mathbf{V}}{\partial z} + \mathbf{v}' \cdot \nabla \mathbf{v}' = -\frac{1}{\rho_\infty} \nabla p' - f \mathbf{k} \times \mathbf{v}' + g \frac{T'}{T_\infty} \mathbf{k} + \nu \nabla^2 \mathbf{v}' \quad (2.12)$$

$$\nabla \cdot \mathbf{v}' = 0, \quad (2.13)$$

where κ is the constant eddy thermometric conductivity and ν is the constant eddy viscosity. A dimensionless form of the equations is used based on the definitions

$$\mathbf{v}'_H = \frac{\mathbf{v}^* \kappa}{z_T - h_{LB}} \quad (2.14)$$

$$w' = \frac{w^* \kappa}{z_T - h_{LB}} \quad (2.15)$$

$$x = x^* L_x \quad (2.16)$$

$$y = y^* L_y \quad (2.17)$$

$$z = z^* (z_T - h_{LB}) + h_{LB} \quad (2.18)$$

$$t = t^* \frac{(z_T - h_{LB})^2}{\kappa} \quad (2.19)$$

$$T' = \frac{T^* \nu \kappa T_\infty}{g (z_T - h_{LB})^3} \quad (2.20)$$

$$p' = \frac{p^* \rho_\infty \kappa^2}{(z_T - h_{LB}) L_x} \quad (2.21)$$

$$\mathbf{V}(z) = |\mathbf{V}(z_T)| \mathbf{V}^*(z^*) \quad (2.22)$$

$$f = \frac{f^* \kappa}{(z_T - h_{LB})^2}. \quad (2.23)$$

These dimensionless equations take the form

$$\frac{\partial T^*}{\partial t^*} = \tilde{\nabla}^2 T^* - Re \mathbf{V}^* \cdot \tilde{\nabla} T^* + Raw^* - \mathbf{v}^* \cdot \tilde{\nabla} T^* \quad (2.24)$$

$$\frac{\partial \mathbf{v}^*}{\partial t^*} = -a_x \tilde{\nabla} p^* + P \tilde{\nabla}^2 \mathbf{v}^* - f^* P \mathbf{k} \times \mathbf{v}^* + PT^* \mathbf{k} \quad (2.25)$$

$$-(Re \mathbf{V}^* + \mathbf{v}^*) \cdot \tilde{\nabla} \mathbf{v}^* - Rew^* \frac{\partial \mathbf{V}^*}{\partial z^*},$$

$$\tilde{\nabla} \times \mathbf{v}^* = 0 \quad (2.26)$$

where

$$\tilde{\nabla} = a_x \frac{\partial}{\partial x^*} \mathbf{i} + a_y \frac{\partial}{\partial y^*} \mathbf{j} + \frac{\partial}{\partial z^*} \mathbf{k}. \quad (2.27)$$

The dimensionless forms lead to two forcing parameters in (2.24)-(2.25). The Reynolds number Re is given by

$$Re = |\mathbf{V}(z_T)| (z_T - h_{LB}) / \kappa \quad (2.28)$$

and represents dynamic forcing by the mean wind shear of the basic state. The Rayleigh number Ra is given by

$$Ra = \frac{g \Delta_z T (z_T - h_{LB})^3}{\nu \kappa T_{00}} \quad (2.29)$$

and represents thermodynamic forcing across the domain.

Three other dimensionless parameters appear in the system. The eddy Prandtl number is defined as

$$P = \nu / \kappa. \quad (2.30)$$

The roll aspect ratios, a_x and a_y , are defined as

$$a_x = \frac{(z_T - h_{LB})}{L_x} \quad (2.31)$$

$$a_y = \frac{(z_T - h_{LB})}{L_y}. \quad (2.32)$$

The vector $\mathbf{V}^*(z^*)$ represents the dimensionless mean wind profile for which $|\mathbf{V}^*(1)| = 1$.

Zuccarello transforms the momentum equation (2.25) by taking the curl to form a vorticity equation, thereby eliminating pressure. The resulting equation is

$$\begin{aligned} \frac{\partial(\tilde{\nabla} \times \mathbf{v}^*)}{\partial t^*} = & P \tilde{\nabla}^2 (\tilde{\nabla} \times \mathbf{v}^*) - f^* P [\tilde{\nabla} \times (\mathbf{k} \times \mathbf{v}^*)] + P (\tilde{\nabla} \times T^* \mathbf{k}) - Re [\tilde{\nabla} \times (\mathbf{V}^* \bullet \tilde{\nabla} \mathbf{v}^*)] \\ & - [\tilde{\nabla} \times (\mathbf{v}^* \bullet \tilde{\nabla} \mathbf{v}^*)] - [\tilde{\nabla} \times (\mathbf{v}^* \bullet \tilde{\nabla} \mathbf{v}^*)] - Re \left[\tilde{\nabla} \times \left(w^* \frac{\partial \mathbf{V}^*}{\partial z^*} \right) \right]. \end{aligned} \quad (2.33)$$

We specify appropriate boundary conditions for the system of equations (2.24) and (2.33). For simplicity, the lateral boundaries are cyclic, and the upper vertical boundary is rigid, stress-free, and perfectly conducting. In contrast, an important source of energy for the circulations exists at the lower boundary; these boundary conditions are specified

using surface layer similarity theory as described in Zuccarello (1994). The vertical boundary conditions are summarized below for $s_T > 0$ and $s_m > 0$, which is consistent with the flow depicted in Fig. 2.1:

$$T^*(0) + s_T \frac{\partial T^*(0)}{\partial z^*} = 0 \quad (2.34)$$

$$u^*(0) - s_m \frac{\partial u^*(0)}{\partial z^*} = 0 \quad (2.35)$$

$$v^*(0) - s_m \frac{\partial v^*(0)}{\partial z^*} = 0 \quad (2.36)$$

$$T^*(1) = 0 \quad (2.37)$$

$$\frac{\partial u^*(1)}{\partial z^*} = \frac{\partial v^*(1)}{\partial z^*} = w^*(1) = 0, \quad (2.38)$$

where s_m , the Schramm momentum constant, and s_T , the Schramm temperature constant, are the similarity parameters as defined in Zuccarello (1994). These parameters control the forcing at the lower vertical boundary. For consistency, the mean wind profile at $z^* = 0$ should satisfy (2.26), (2.35) and (2.36). As a consequence of (2.26), (2.35) and (2.36), we get

$$\frac{\partial w^*(0)}{\partial z^*} - s_m \frac{\partial^2 w^*(0)}{\partial z^{*2}} = 0 \quad (2.39)$$

Note that this equation does not handle the vertical velocity at the lower boundary as we would like, but rather it involves derivatives of the vertical velocity.

2.1.2. The Spectral System

Zuccarello used the Galerkin technique or spectral method to form a spectral model. We use Fourier expansions for the variables that were determined by a suitable eigenvalue problem using the above boundary conditions. The Galerkin method applied to (2.24) and (2.33) yields a nonlinear dynamical system (NDS). We then truncate the NDS to 60 equations based on 20 variable amplitudes for temperature and 40 for velocity. Each partial differential equation term may be represented by the product of a 60×60 matrix and a 60-element vector representing the 60 amplitude coefficients. The resulting NDS takes the form

$$A\dot{y} = By + C(y)y, \quad (2.40)$$

where A is a 60×60 invertible matrix of inner products multiplying the 60-element vector \dot{y} that contains the temporal derivatives of the amplitude coefficients, B is a 60×60 constant matrix, arising from the linear terms of the partial differential equations, multiplying the 60-element vector y that contains the amplitude coefficients, and C is a 60×60 linear-in- y matrix, based on the advective terms of the partial differential equations, multiplying the same 60-element vector y . Because A is invertible, we may solve for the time-dependent amplitude coefficients by numerically integrating the following system:

$$\dot{y} = A^{-1}By + A^{-1}C(y)y. \quad (2.41)$$

The truncated Fourier expansion for the dependent variable T^* is composed of temporally dependent amplitudes, spatially dependent trigonometric functions with horizontal wavenumbers l and m , and vertical basis functions:

$$T^*(x^*, y^*, z^*, t^*) = \sum_{i=0}^4 \sum_{j=1}^4 T_{ij}(t^*) \text{trig}_i(x^*, y^*) F_j(z^*), \quad (2.42)$$

where

$$\text{trig}_0(x^*, y^*) = 1 \quad (2.43)$$

$$\text{trig}_1(x^*, y^*) = \sin 2\pi l x^* \sin 2\pi m y^* \quad (2.44)$$

$$\text{trig}_2(x^*, y^*) = \sin 2\pi l x^* \cos 2\pi m y^* \quad (2.45)$$

$$\text{trig}_3(x^*, y^*) = \cos 2\pi l x^* \sin 2\pi m y^* \quad (2.46)$$

$$\text{trig}_4(x^*, y^*) = \cos 2\pi l x^* \cos 2\pi m y^* \quad (2.47)$$

$$F_1(z^*) = \cosh \omega_1 z^* - \frac{1}{s_T \omega_1} \sinh \omega_1 z^* \quad \text{for } s_T < 1 \quad (2.48)$$

$$F_1(z^*) = \cos \omega_1 z^* - \frac{1}{s_T \omega_1} \sin \omega_1 z^* \quad \text{for } s_T > 1 \quad (2.49)$$

$$s_T \omega_1 = \tanh \omega_1 \quad \text{for } s_T < 1 \quad (2.50)$$

$$s_T \omega_1 = \tan \omega_1 \quad \text{for } s_T > 1 \quad (2.51)$$

$$F_j(z^*) = \cos \omega_j z^* - \frac{1}{s_T \omega_j} \sin \omega_j z^* \quad \text{for } j = 2, 3, 4 \quad (2.52)$$

$$s_T \omega_j = \tan \omega_j \quad \text{for } j = 2, 3, 4, \quad (2.53)$$

and the vertical basis functions $F_i(z^*)$ are orthogonal.

The expansion for the velocity vector \mathbf{v}^* is more complex. Because it is nondivergent, \mathbf{v}^* is represented (nonuniquely) by the curl of a vector streamfunction \mathbf{A}^*

that is the sum of two vector streamfunctions ψ^* and η^* . Therefore, we express the velocity perturbation vector \mathbf{v}^* as

$$\mathbf{v}^* = \nabla \times \mathbf{A}^* = \nabla \times \psi^* + \nabla \times \eta^*. \quad (2.54)$$

We use a truncated Fourier expansion, similar to that for T^* , to represent the dependent vector streamfunctions ψ^* and η^* :

$$\psi^*(x^*, y^*, z^*, t^*) = \sum_{p=0}^4 \sum_{q=1}^4 \psi_{pq}(t^*) \text{trig}_p(x^*, y^*) h_q(z^*) \mathbf{i} + 0\mathbf{j} + 0\mathbf{k} \quad (2.55)$$

$$\eta^*(x^*, y^*, z^*, t^*) = 0\mathbf{i} + \sum_{p=0}^4 \sum_{q=1}^4 \eta_{pq}(t^*) \text{trig}_p(x^*, y^*) h_q(z^*) \mathbf{j} + 0\mathbf{k}, \quad (2.56)$$

where $\text{trig}_p(x^*, y^*)$ is defined in (2.43)-(2.47), and

$$h_q(z^*) = \cos \varpi_q z^* - s_m \varpi_q \sin \varpi_q z^* \quad \text{for } q = 1, 2, 3, 4 \quad (2.57)$$

$$s_m \varpi_q = \cot \varpi_q \quad \text{for } q = 1, 2, 3, 4, \quad (2.58)$$

where the vertical basis functions $h_q(z^*)$ are nonorthogonal.

During the Galerkin process, the expansions are put into the appropriate terms in the dimensionless partial differential equations, multiplied by appropriate individual basis functions, and then simplified by integrating the trigonometric functions in the expansions and using appropriate identities.

2.2. Energetics Analysis

In Zuccarello (1994), it is hypothesized that computer runs of the model there fail to converge because of an unknown energy source. Here, we performed an energetics analysis to determine all the energy sources and sinks in the system. Using the thermodynamic equation and the equation of motion, we can determine the energy rate equations for the system. These energy rate equations are composed of obvious energy sources and sinks, as well as boundary terms that can be either sources or sinks. By properly choosing the boundary conditions, we can eliminate most of the boundary terms and so simplify the energy rate equations. Using energetics analysis as a diagnostic tool, we determine whether our current boundary conditions adequately control the system energetics. Appendix A fully describes the energetics analysis.

In the first step in the energetics analysis, we calculate the kinetic energy (KE) rate equation from the equation of motion. We multiply the equation of motion (2.25) by the velocity vector \mathbf{v}^* and then take the volume integral of the product. The result of the vector dot product, integration by parts, introduction of the boundary conditions (2.34) - (2.39), and integration over z^* when possible, is:

$$\begin{aligned}
 \dot{KE} = & \int_B -a_x w^* p^*|_{z^*=0} dB - \int_V P \left(a_k \delta_{ki} \frac{\partial v_j^*}{\partial x_i} \right)^2 dV - \int_B P \left(\frac{u^{*2}}{s_m} + \frac{v^{*2}}{s_m} + w^* \frac{\partial w^*}{\partial z^*} \right) \Big|_{z^*=0} dB \\
 & (1) \qquad (2) \qquad (3) \\
 & + \int_V PT^* w^* dV + \int_B \frac{w^* v_i^{*2}}{2} \Big|_{z^*=0} dB - \int_V Rew^* v_i^* \frac{\partial V_i^*}{\partial z^*} dV, \qquad (2.59) \\
 & (4) \qquad (5) \qquad (6)
 \end{aligned}$$

where \dot{KE} is the KE rate of change and B is the horizontal boundary.

The six terms on the right side of (2.59) represent sources and sinks of energy. The first term is a boundary term due to pressure work. The second term is traditionally the KE dissipation term and is clearly an energy sink. The third and fifth terms are also boundary terms. The three boundary terms (1), (3), and (5) are either energy sources or sinks depending on the sign of the velocity term within the integral and the sign of the Schramm constant s_m in term (3) (for this model $s_m > 0$). The fourth term is a convective energy source term describing the conversion of AE to KE . We denote it as $C(AE, KE)$. The last term (6) is a KE generation or Reynolds stress term representing the dynamic source of energy.

Next, we calculate the available energy (AE) rate equation (\dot{AE}) from the thermodynamic equation (2.24) and the $C(AE, KE)$ term in (2.59). We need the same conversion term, but with the opposite sign, in the \dot{AE} equation. Therefore, we add and subtract the required term in order to introduce it appropriately. We derive the \dot{AE} equation by multiplying the volume integral of the thermodynamic equation by an appropriate factor to obtain $-C(AE, KE)$ from the modified convection term. After integrating by parts, applying the boundary conditions (2.34) - (2.39), and integrating over z^* when possible, we get the \dot{AE} equation:

$$\begin{aligned}
 \dot{AE} = & \int_B \frac{T^{*2}}{s_T} \Big|_{z^*=0} dB - \int_V P \left(a_k \delta_{ki} \frac{\partial T^*}{\partial x_i^*} \right)^2 dV + \int_V (Ra + 1) PT^* w^* dV \\
 & \quad (1) \qquad \qquad \qquad (2) \qquad \qquad \qquad (3) \\
 & - \int_V PT^* w^* dV + \int_B \frac{PT^{*2} w^*}{2} \Big|_{z^*=0} dB. \qquad \qquad \qquad (2.60) \\
 & \quad (4) \qquad \qquad \qquad (5)
 \end{aligned}$$

The six terms on the right side of (2.60) represent sources and sinks of AE . The first term is a boundary term that depends on the sign of the temperature Schramm constant, s_T . We use $s_T > 0$ in this model, so term (1) is an AE source. The second term is an AE dissipation term and is clearly a sink. The third term comes from the original Rayleigh term in the thermodynamic equation and our correction term. Assuming that T^* and w^* should be positively correlated, the third term is an AE source for $Ra > -1$ and a sink for $Ra < -1$. The case of $Ra = -1$ corresponds to a thermodynamically neutral atmosphere as no thermal energy arising from the mean lapse rate $\Delta_z T / z_T$ can be converted to KE . In term (4), we find the $C(AE, KE)$ term of the \dot{KE} equation, but with the opposite sign. It represents a source or sink of AE , but not a net source of total energy $KE+AE$. The last term is another boundary term, and, depending on the sign of the vertical velocity at $z^* = 0$, is either a source or sink of AE .

We have completed the energetics analysis for the original equations of the problem, but the model uses the vorticity equation (2.33). Therefore, we need to continue the analysis by examining the \dot{KE} equation derived from the vorticity equation. For physical consistency, we must obtain the same \dot{KE} equation found from the equation of motion (2.59). However, we cannot get this form by multiplying (2.33) by the velocity perturbation, \mathbf{v}^* . To get the correct form, we multiply the vorticity equation by the vector streamfunction \mathbf{A}^* and then take the volume integral (see Appendix A for details). The result, after vector multiplication, integration by parts, application of the boundary conditions (2.34) - (2.39), and integration over z^* when possible, is:

$$\dot{KE} = - \int_V P \left(a_k \delta_{ki} \frac{\partial v_j^*}{\partial x_i} \right)^2 dV - \int_B P \left(\frac{u^{*2}}{s_m} + \frac{v^{*2}}{s_m} + w^* \frac{\partial w^*}{\partial z^*} \right) \Big|_{z^*=0} dB$$

(2)

(3)

$$+ \int_V PT^* w^* dV + \int_B \frac{w^* v_i^{*2}}{2} \Big|_{z^*=0} dB - \int_V Rew^* v_i^* \frac{\partial V_i^*}{\partial z^*} dV$$

(4)

(5)

(6)

$$+ \int_B A_i \frac{\partial}{\partial t^*} \frac{\partial A_i}{\partial z^*} \Big|_{z^*=0} dB - \int_B PA_i a_k^2 \delta_{ki} \frac{\partial^2}{\partial x_j^{*2}} \frac{\partial A_i}{\partial z^*} \Big|_{z^*=0} dB + \int_B \varepsilon_{3jk} f^* PA_k \frac{\partial A_j}{\partial z^*} \Big|_{z^*=0} dB$$

(7)

(8)

(9)

$$+ \int_B ReA_i V_j^* a_k \delta_{kj} \frac{\partial}{\partial x_j^*} \frac{\partial A_i}{\partial z^*} \Big|_{z^*=0} dB - \int_B \varepsilon_{i3j} ReA_i w^* \frac{\partial V_j^*}{\partial z^*} \Big|_{z^*=0} dA$$

(10)

(11)

$$+ \int_B \varepsilon_{ijk} A_l a_m \delta_{mj} \frac{\partial A_k}{\partial x_j^*} a_n \delta_{ni} \frac{\partial}{\partial x_i^*} \frac{\partial A_l}{\partial z^*} \Big|_{z^*=0} dB, \quad (2.61)$$

(12)

where the tensor A_k is the streamfunction component ψ^* when $k = 1$, η^* when $k = 2$, and 0 when $k = 3$.

A quick comparison of (2.59) and (2.61) shows the two \dot{KE} equations are quite different. However, a closer look reveals some interesting results. We do not find term (1), the pressure boundary term of (2.59), directly in (2.61). However, we find the next

five terms in both (2.59) and (2.61). The terms are: the dissipation term (2); a boundary term (3); the $C(AE, KE)$ term (4); another boundary term (5); and the KE generation term (6). We can find no direct comparison in (2.59) with the six remaining terms in (2.60). Therefore, these six terms must come from the pressure boundary term in (2.58), since these two equations must be equal and the pressure boundary term is the only term not found in (2.61).

The last six terms in (2.61) are boundary terms, as is the pressure work term in (2.59). As stated earlier, if we choose our boundary conditions correctly then we can eliminate most of the boundary terms in the energy rate equations. Besides these related terms, terms (3) and (5) are boundary terms in the \dot{KE} equations, and term (5) is a boundary term in the \dot{AE} equation. Examining all the boundary terms reveals a dependence on the vertical velocity w^* and the stream function A_k^* at $z^* = 0$. We chose the simplest new boundary condition that eliminates most of these terms:

$$A_k^*(z^* = 0) = 0. \quad (2.62)$$

As a consequence of (2.62), we get

$$w^*(z^* = 0) = 0. \quad (2.63)$$

Before accepting these simple and obvious boundary conditions, we make sure that they represent observed atmospheric conditions. It could be argued that the vertical velocity perturbation at 10 *m* above the sea surface is not identically zero. However, with typical scaling arguments, we can show that the vertical velocity perturbation is negligible when compared with the horizontal velocity perturbations. Additionally, we do not need

a nonzero vertical velocity to transfer the momentum and heat flux to the surface, since smaller scale eddies are responsible for this transfer.

The two additional boundary conditions help solve Zuccarello's problems of an unknown energy source and a maximum vertical velocity at the lower boundary. The new boundary conditions eliminate the many possible, unrealistic boundary energy sources and they control the vertical velocity at the lower boundary. The first boundary condition (2.62) also helps to move the maximum momentum flux higher into the boundary layer. The horizontal velocities are curls of the two streamfunctions in (2.54) and have z -derivatives of the streamfunction in their definitions. Therefore, boundary condition (2.62) does not force the horizontal velocities to zero, but it does reduce them. This reduction of horizontal velocity and our control of the vertical velocity at the lower boundary forces the maximum momentum flux to occur higher in the boundary layer.

The addition of these two boundary conditions reduces the energetics to:

$$\dot{KE} = - \int_V P \left(a_k \delta_{ki} \frac{\partial v_i^*}{\partial x_i} \right)^2 dV - \int_B P \left(\frac{u^{*2}}{s_m} + \frac{v^{*2}}{s_m} \right) \Big|_{z^*=0} dB + \int_V PT^* w^* dV \quad (2.63)$$

$$- \int_V Re w^* v_i^* \frac{\partial V_i^*}{\partial z^*} dV \quad (2.64)$$

$$\dot{AE} = \int_B \frac{T^{*2}}{s_T} \Big|_{z^*=0} dB - \int_V P \left(a_k \delta_{ki} \frac{\partial T^*}{\partial x_i} \right)^2 dV + \int_V (Ra + 1) PT^* w^* dV - \int_V PT^* w^* dV \quad (2.65)$$

The terms in the \dot{KE} equation are: KE dissipation (1), a boundary KE sink term (2) (since $s_m > 0$), the $C(AE, KE)$ term (3), and the KE generation term (4). Similar terms are in the \dot{AE} equation: a boundary AE source term (1) (since $s_r > 0$), the AE dissipation term (2), the AE generation term (3), and the $C(AE, KE)$ term (4). Note that boundary layer flow driven by heat flux from the bottom and modified only by shear within the boundary layer occurs when $Ra = -1$. We examine this special case in Chapter 3.

2.3. Incorporation of New Boundary Conditions

The addition of two new boundary conditions (2.62) - (2.63) to the original Monin-Obukhov boundary conditions (2.34) - (2.39), greatly changes our system of equations. However, we did not want to completely rederive and rewrite the model at this time. Instead we were able to adjust the existing system with some minor changes to the vertical expansion functions for the streamfunctions that now satisfy both new boundary conditions.

We apply the new boundary conditions at the lower boundary $z^* = 0$. So we start by examining the vector streamfunction \mathbf{A}^* using (2.55) and (2.56):

$$\begin{aligned} \mathbf{A}^*(x^*, y^*, z^*, t^*) = \sum_{p=0}^4 \sum_{q=1}^4 \left[\left\{ \psi_{pq}(t^*) \text{trig}_p(x^*, y^*) h_q(z^*) \right\} \mathbf{i} \right. \\ \left. + \left\{ \eta_{pq}(t^*) \text{trig}_p(x^*, y^*) h_q(z^*) \right\} \mathbf{j} + 0\mathbf{k} \right]. \end{aligned} \quad (2.66)$$

The only dependence on z^* in (2.66) is in the vertical basis function $h_q(z^*)$. If we want $\mathbf{A}^*(z^* = 0) = 0$, then we must force $h_q(0) = 0$, for each of the four vertical wavenumbers q .

However, using the definition of $h_q(z^*)$ in (2.57), we find its value for each of the four vertical wavenumbers at the lower boundary is:

$$h_q(0) = 1. \quad (2.67)$$

From (2.67) we see a very simple way to make the new vertical basis functions vanish leading to $\mathbf{A}^*(z^* = 0) = 0$. We define new vertical basis functions $h_{newq'}$, for $q' = 1, 2, 3$, by taking appropriate differences of the old basis functions $h_{oldq} = h_q$:

$$h_{new1} = h_{old1} - h_{old2} \quad (2.68)$$

$$h_{new2} = h_{old2} - h_{old3} \quad (2.69)$$

$$h_{new3} = h_{old3} - h_{old4}. \quad (2.70)$$

The three new vertical basis functions reduce the number of vertical wavenumbers in the streamfunction representation from four to three. We use (2.57) to define the old basis functions and then use these values to obtain the new basis functions (2.68) - (2.70).

Once put into a new Galerkin expansion, the resulting new function satisfies the boundary condition $\mathbf{A}^*(z^* = 0) = 0$:

$$\begin{aligned} \mathbf{A}^*(x^*, y^*, z^*, t^*) = & \sum_{p=0}^4 \sum_{q'=1}^3 \left[\left\{ \psi_{pq'}(t^*) \text{trig}_p(x^*, y^*) h_{newq'}(z^*) \right\} \mathbf{i} \right. \\ & \left. + \left\{ \eta_{pq'}(t^*) \text{trig}_p(x^*, y^*) h_{newq'}(z^*) \right\} \mathbf{j} + 0\mathbf{k} \right]. \end{aligned} \quad (2.71)$$

Substituting (2.68)-(2.70) in (2.71) yields

$$\begin{aligned} \mathbf{A}^*(x^*, y^*, z^*, t^*) = & \sum_{p=0}^4 \sum_{q'=1}^3 \left[\left\{ \psi_{pq'}(t^*) \text{trig}_p(x^*, y^*) (h_{oldq'}(z^*) - h_{oldq'+1}(z^*)) \right\} \mathbf{i} \right. \\ & \left. + \left\{ \eta_{pq'}(t^*) \text{trig}_p(x^*, y^*) (h_{oldq'}(z^*) - h_{oldq'+1}(z^*)) \right\} \mathbf{j} + 0\mathbf{k} \right]. \end{aligned} \quad (2.72)$$

At $z^* = 0$, the old basis functions $h_{oldq} = 1$ by (2.67) and therefore their differences in (2.72) cancel. Summing over p and q' results in $\mathbf{A}^*(z^* = 0) = 0$.

When we calculate the curl of \mathbf{A}^* in (2.71), we get the new velocity component equations. The vertical velocity expansion is:

$$\begin{aligned} w^*(x^*, y^*, z^*, t^*) = & \sum_{p=0}^4 \sum_{q'=1}^3 \left[\eta_{pq'}(t^*) \frac{\partial}{\partial x^*} \text{trig}_p(x^*, y^*) h_{newq'}(z^*) \right. \\ & \left. - \psi_{pq'}(t^*) \frac{\partial}{\partial y^*} \text{trig}_p(x^*, y^*) h_{newq'}(z^*) \right]. \end{aligned} \quad (2.73)$$

Summing over p and q' , we get $w^*(0) = 0$, which is our other new boundary condition.

Appendix B offers a closer look at incorporating these new boundary conditions into our system of equations.

2.4. The Computer Model

The computer code used to represent the physical and mathematical model presented in the previous sections is written in the FORTRAN programming language. It is compiled using the WATFOR77 compiler. The first part of the code determines the

values for ω_j for $j = 1, 2, 3, 4$, and ϖ_q for $q = 1, 2, 3, 4$, based on input values of the constants s_m and s_T . The values of these constants are provided by the subroutine discussed in Appendix A of Zuccarello (1994). An iterative technique is used to solve (2.50)-(2.51), (2.53), and (2.58) for the eigenvalues. Zuccarello suggests that for new values of s_m and s_T , a new set of eigenvalues be put into the model as a seed set for the iterative process. However, after running several different cases with different values of s_m and s_T , we find the iterative process adequately yields the new eigenvalues from a single seed set. Prior to integrating the system, we choose values for the parameters l, m, a_x, a_y, Ra, Re , and P .

The above parameter values are used to fill the matrices representing the terms in the NDS. The individual matrices that compose A , B , and C in (2.39) are grouped as temporal derivative term matrices, linear term matrices, and nonlinear term matrices, respectively. The temporal derivative term matrix A and the linear term matrix B are determined prior to the integration because A and B do not depend on the spectral coefficient in y . An IMSL routine computes A^{-1} and a different IMSL routine computes $A^{-1}B$. The nonlinear term matrix must be calculated during each integration time step because C depends on y . The calculation of $A^{-1}C(y)$ may also be done during each time step.

During a preliminary linear analysis of the model, we discovered a problem with $A^{-1}B$. There were some terms in the matrix that should be zero because of algebraic cancellation. However, owing to round-off errors, the values of these terms had values on the order of 10^{-16} to 10^{-18} . In scaling arguments, we would normally take these numbers to be zero, but the IMSL subroutine we use for the linear analysis did not. When we perform eigenvalue analyses of the temperature and vorticity dissipation terms, which appear only on the diagonal of the matrix, we expected to get only real eigenvalues.

Instead we obtained complex eigenvalues because of the small nonzero terms in the matrix. We solved this problem by copying all the terms that were supposed to be nonzero into another matrix filled with zeros.

When we defined the new vertical basis function $h_{newq'}$, we reduced the streamfunction vertical wavenumbers from four to three. This result reduces the number of model equations and coefficients from 60 to 50. Therefore, we rewrote the parts of the model, involving the vertical basis functions, using the new definitions (2.68) - (2.70) and construct A , B and C as 50×50 matrices.

The IMSL integration routine uses the Adams-Gear method and requires user-supplied initial conditions for the 50-element vector y . At each time step, an IMSL routine calculates $A^{-1}By$ and $A^{-1}C(y)y$. The resulting 50-element vectors from the linear and nonlinear matrices are added together to give the right sides of the 50 equations for which we are solving.

The integration routine uses these results to calculate new values for the 50 time-dependent amplitude coefficients after each time step. We integrate the model until the square root of the sum of the squares of the coefficients equilibrates. After the model integration is complete, these amplitude coefficients are used to construct the model solution using (2.42), (2.54) and (2.71). Examples of this solution are given in the following chapter.

Chapter 3

HI-RES CASE STUDY

We evaluate the model with the new boundary conditions by performing a series of model analyses and integrations using observed marine atmospheric boundary layer (MABL) data from 1993 Hi-Res 2 field experiment to calculate the model parameter values. This experiment yielded coincident ship measurements of the atmospheric and oceanic state and synthetic aperture radar (SAR) imagery from ERS-1 (Sikora *et al.* 1995). The analyses include linear studies using different physical parameter values and wind profiles. We determine the preferred physical parameter values for our case study using linear eigensystem evaluations (Laufersweiler 1987). The examination of the preferred physical parameter values yields a set of aspect ratios associated with a bifurcating, temporally periodic solution. We then perform some integrations using several sets of these preferred, physical parameter values and initial conditions. After the integrations, the analyses include energy conservation checks on the model solutions and graphical representations of the evolution of the solution. We use these integrations to locate code errors and to fine-tune the model parameters.

Using one set of aspect ratios, we perform the Hi-Res 2 case study to investigate the solutions for boundary layer spanning eddies (BLSE). These eddies are composed of component circulations parallel to the mean wind and perpendicular to the mean wind; both roll circulations and cellular ones are represented. We examine the BLSE surface-stress patterns produced by the model and compare them with the pattern observed in our case study Hi-Res 2 SAR imagery. We also compare the results with those of other models to assess both the performance of our model and the effects of incorporating the forcing rates in the lower vertical boundary conditions. We describe the Hi-Res 2 data in

Section 3.1 and present the case study data and analyses yielding the preferred physical parameter values in Section 3.2. The results of this case study are given in Section 3.3.

3.1. Description of Hi-Res 2 Data

The observed data for our case study are from the Hi-Res 2 field experiment conducted during June 1993. The Hi-Res cruise coincided with SAR imaging from the European Remote Sensing Satellite ERS-1 off the coast of North Carolina. From 16 June to 18 June 1993, the R/V Columbus Iselin and the R/V Bartlett collected observations at the sea-surface and at $z = 10\text{ m}$ within the area enclosed by the coordinates $35.2^\circ - 36.6^\circ$ N and $73.8^\circ - 75.0^\circ$ W. We examined an ERS-1 SAR composite image, published by Sikora *et al.* (Figure 1, 1995), dated 1538 GMT 17 June 1993 that covered this same area.

Sikora *et al.* (1995) found two distinct patterns on this image. They concluded that the mottled pattern on this image, south of the Gulf Stream North Wall (GSNW), is the signature of convectively driven BLSE, while the marbled pattern, north of the GSNW, is the signature of a stable MABL. Using these criteria, we chose to study the convective region near 35.8° N, 74.2° W that displays an alternating dark/light pattern with an apparent kilometer-scale wavelength. The R/V Columbus Iselin researchers recorded surface observations, kindly shared with us by Dr. Jim Edson of Woods Hole Oceanographic Institution, in this region near the time of the SAR image.

The meteorological conditions in the Hi-Res region at this time were relatively quiet. According to Sikora *et al.* (1995), the 1500 GMT 17 June 1993 National Meteorological Center (NMC) surface analysis indicates that the imaged area was located within a uniform, relatively warm air mass south of a stationary front. The NMC upper air analysis from 1200 GMT 17 June 1993 shows the imaged area to be just east of a

large, upper-air ridge (Sikora *et al.* 1995). Also, Sikora *et al.* (1995) report that observation notes from meteorological personnel aboard the R/V Columbus Iselin indicate a dramatic atmospheric meso-front occurred in the vicinity of the GSNW.

The absence of any synoptic-scale disturbances suggests that locally driven BLSE are responsible for the imaged stress patterns (Sikora *et al.* 1995). The R/V Columbus Iselin data from over the Gulf Stream displays a distinct air/sea temperature difference, with sea-surface temperatures (SST) greater than the air temperatures in the region of marbled sea-surface patterns. This air/sea temperature difference is one of the mechanisms for BLSE described in Chapter 2 and modeled here.

3.2. Case Study Data and Preferred Parameter Values

The meteorological staff onboard the R/V Columbus Iselin took observations an average of three to four times an hour on 17 June. We average these observations for each hour (Table 3.1). The R/V Columbus Iselin was in the vicinity of our case study point, 35.8° N, 74.2° W, from 1400 GMT 17 June through 0000 GMT 18 June. Since observations were taken at 10 m, we chose $z = h_{LB} = 10\text{ m}$. The observed wind measurements were relative to the fixed Earth. We subtract the observed current from the observed winds to make the wind velocity relative to the ocean — U_{Rel} and V_{Rel} . We infer the mixing ratio at the sea surface by assuming that the air is saturated at this level. We use the averages of all the observed parameter values over each hour to specify the model parameter values for a case, Table 3.1. (Note: the observed data shared with us did not include any 1700 GMT and 2000 GMT 17 June data.)

Table 3.1. Hi-Res 2 Observed MABL data. Note: 1700 GMT and 2000 GMT data not available.

Hour	Wind	Wind	U	V	Ocean	Ocean	Ocean	Ocean	U Rel	V Rel
	Speed	Direction	Relative to Earth		Current	Curr Dir	Curr Dir		Relative to Current	
	10 m	10 m	10 m	10 m				10 m	10 m	10 m
(GMT)	(m/s)	(degrees)	(m/s)	(m/s)	(m/s)	OCEAN	METEO	(m/s)	(m/s)	(m/s)
14	2.23	250.73	2.11	0.74	1.58	38.87	218.87	1.11	-0.48	
15	1.80	255.77	1.74	0.44	1.55	80.58	188.58	1.08	-0.24	
16	1.35	267.73	1.35	0.05	1.60	43.82	223.82	0.24	-1.10	
18	2.04	229.89	1.48	1.33	1.65	93.70	183.70	0.88	0.77	
19	3.66	229.11	2.58	2.42	1.59	44.54	224.54	1.46	1.30	
21	5.13	211.82	2.70	4.35	1.66	47.80	227.80	1.48	3.24	
22	4.69	213.25	2.57	3.92	1.75	49.12	229.12	1.25	2.77	
23	3.90	208.93	1.87	3.41	2.00	43.94	223.94	0.48	1.97	

Hour	Water Temp.	Air Temp.	Mixing Ratio	Mixing Ratio	Mixing Ratio	Schramm Constant	Surface	M-O
	SST	T10	q10	qsea (Inferred)	Thermal	Length		
	Sea Surface	10 m	10 m	Sea Surface	s_m	s_T	Roughness	L
(GMT)	(C)	(C)	(g/Kg)	(g/Kg)			z_0	(m)
14	26.82	24.35	13.53	22.00	0.425	1.144	0.371×10^{-4}	-0.682
15	27.87	24.96	13.57	23.00	0.438	1.226	0.374×10^{-4}	-0.570
16	27.75	25.03	13.60	23.00	0.563	2.665	1.011×10^{-4}	-0.043
18	28.03	25.23	13.24	23.00	0.459	1.385	0.426×10^{-4}	-0.399
19	27.33	25.38	13.70	22.33	0.388	0.928	0.319×10^{-4}	-1.260
21	27.83	25.50	14.66	22.75	0.391	0.921	0.316×10^{-4}	-1.206
22	27.98	25.49	14.32	23.00	0.411	1.065	0.345×10^{-4}	-0.833
23	28.11	25.33	13.92	23.00	0.509	1.891	0.646×10^{-4}	-0.149

The physical parameter values from Table 3.1 — U_{Rel} , V_{Rel} , SST , $T10$, q_{sea} , $q10$ — are input into the subroutine described in Appendix A of Zuccarello (1994). This subroutine determines values for the surface roughness, z_0 , and the Monin-Obukhov length, L . The values obtained for z_0 and L are then used in another subroutine that calculates values for the two constant lower boundary Schramm forcing parameters, s_m and s_T . The values for z_0 , L , s_m and s_T calculated from the different Hi-Res data points are found in Table 3.1. Our values of L agree with those in Sikora *et al.* (1995). The range of values of s_m and s_T for 17 June are exponentially related, as shown in Fig. 3.1.

From Table 3.1, we chose the averaged 1900 GMT data for our case study. During this time period, the R/V Columbus Iselin was in the middle of the dark/light pattern on the SAR image. This pattern is oriented 35° west of north and has horizontal spacing of approximately 1000 m. The parameter values for s_m and s_T (darkened square in Fig. 3.1) are typical of those values characterizing the state of the 17 June MABL. The relative winds at $z = 10$ m were 2 ms^{-1} from the southwest. We plot the value of the relative winds and the air/sea temperature difference on Woodcock's (1975) regime diagram in Fig. 3.2. The regime diagram indicates that the 1400-2400 GMT averaged data are in the three-dimensional cell region (1900 GMT point is darkened diamond). The 1900 GMT upper air sounding, taken from the R/V Columbus Iselin during this time, showed an inversion base height of 900 m. This inversion base height defines our upper boundary height $z_T = 900$ m. The expected aspect ratios for the observed spacing on the SAR image are thus $a_x = 0.73$ and $a_y = 0.51$. The sounding winds were not available through the boundary layer. However, researchers on board the R/V Columbus Iselin noted that the wind speeds were light through the boundary layer.

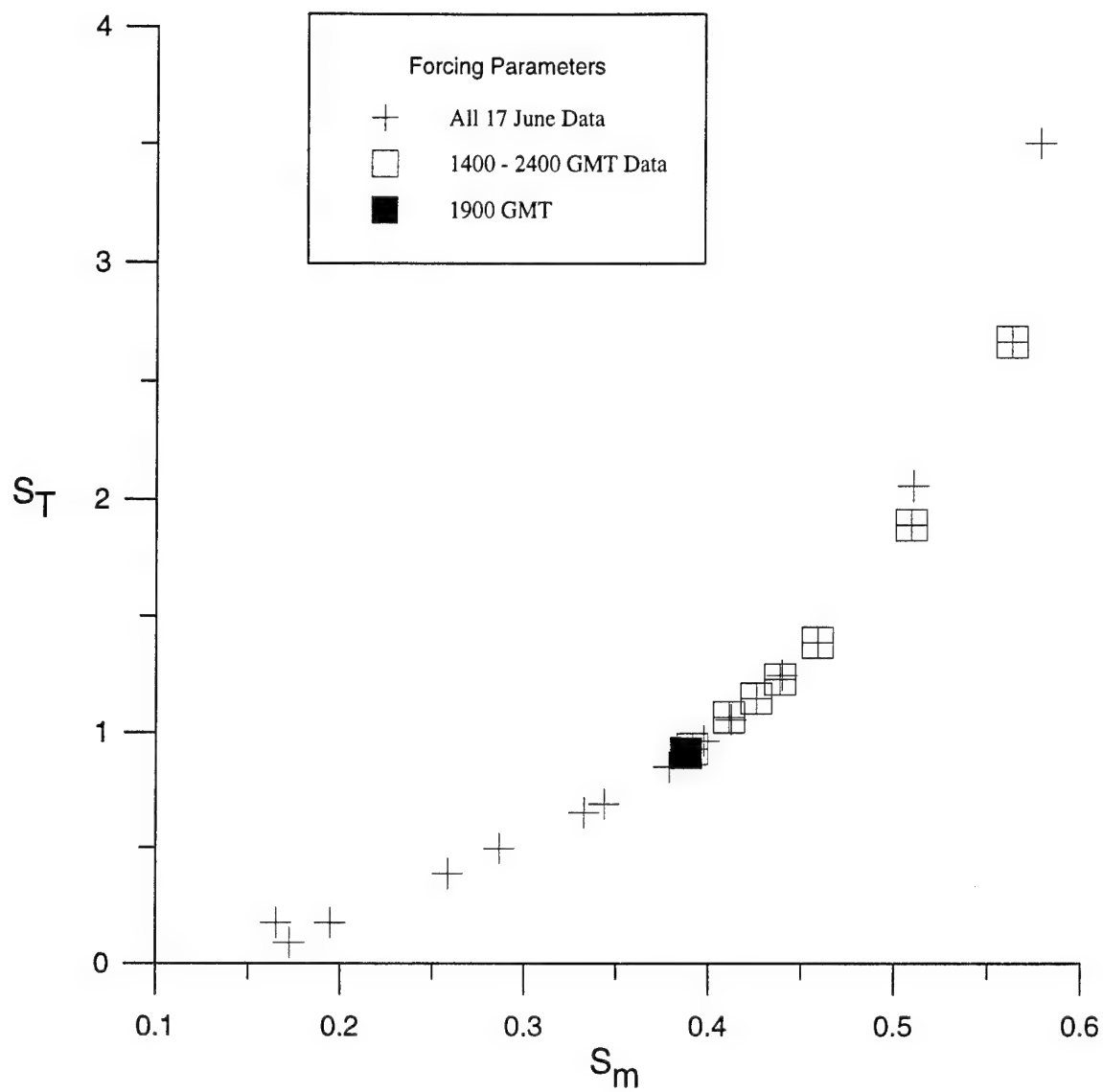


Fig. 3.1. Range of values of s_m and s_T for 17 June 1993 calculated from R/V Columbus Iselin observations. Highlighted values are from Table 3.1 data.

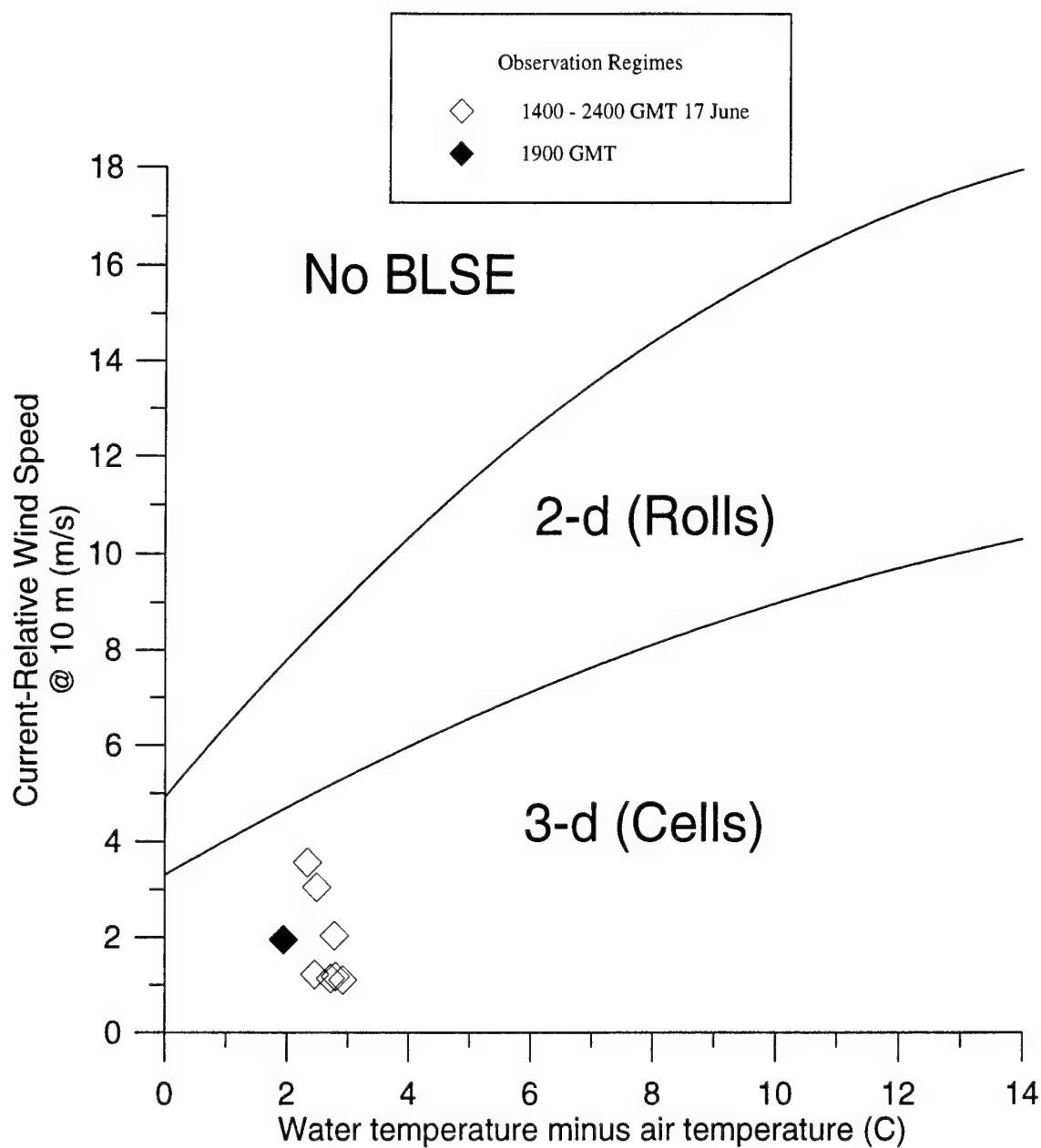


Fig. 3.2 Woodcock (1975) diagram determines circulation regimes from relative wind speed and air/sea temperature difference. The curves are derived from observations of seagulls over the ocean. The diamonds represent the points using the data in Table 3.1.

Rather than use a constant wind profile, we use formulas which we may fit to natural boundary conditions and to winds observed at the surface and aloft. Since the winds aloft are not known, we use the following formulas for the profiles $U(z)$ and $V(z)$

$$U(z) = a_U z + b_U z^{2/3} + c_U z^{1/3} + d_U. \quad (3.1)$$

$$V(z) = a_V z + b_V z^{2/3} + c_V z^{1/3} + d_V. \quad (3.2)$$

We use (2.14) - (2.23) to make these profiles dimensionless. We require that the mean wind profiles satisfy the same boundary conditions that the perturbation wind velocity satisfies. These boundary conditions are

$$U^*(z^* = 0) - s_m \frac{\partial U^*(z^* = 0)}{\partial z^*} = 0, \quad V^*(z^* = 0) - s_m \frac{\partial V^*(z^* = 0)}{\partial z^*} = 0, \quad (3.3)$$

$$U^*(z^* = 0) = U_{Rel} / |\mathbf{V}_{Top}|, \quad V^*(z^* = 0) = V_{Rel} / |\mathbf{V}_{Top}|, \quad (3.4)$$

$$U^*(z^* = 1) = U_{Top} / |\mathbf{V}_{Top}|, \quad V^*(z^* = 1) = V_{Top} / |\mathbf{V}_{Top}|.$$

Since the mean wind varies only in the vertical direction, it is also incompressible. We obtain the Reynolds number Re through its definition (2.27). In (3.3) - (3.4) we then use the values from Table 3.1 for s_m , U_{Rel} , and V_{Rel} at $z = h_{LB} = 10 \text{ m}$ ($z^* = 0$) to solve for the variables a_U, b_U, c_U, a_V, b_V , and c_V in (3.1) and (3.2). The variables d_U and d_V are free variables that we use to control the shear and turning in the profile. We use an EXCEL spreadsheet to calculate and plot the profiles for different values of Re and the free variables d_U and d_V prior to inputting them into the model.

Table 3.2. Parameter values used in case study.

PARAMETER	VALUE
HEIGHT OF TOP OF DOMAIN (Z_T)	900 m
HEIGHT OF BOTTOM OF DOMAIN (h_{LB})	10 m
ASPECT RATIO IN THE X-DIRECTION (a_x)	0.56
ASPECT RATIO IN THE Y-DIRECTION (a_y)	0.38
REYNOLDS NUMBER (Re)	250.0
U MEAN WIND SPEED AT $Z = Z_T$	1.46 m s^{-1}
U MEAN WIND SPEED AT $Z = h_{LB}$	1.99 m s^{-1}
V MEAN WIND SPEED AT $Z = Z_T$	1.30 m s^{-1}
V MEAN WIND SPEED AT $Z = h_{LB}$	1.99 m s^{-1}
U MEAN WIND PROFILE PARAMETER (d_U)	1.40
V MEAN WIND PROFILE PARAMETER (d_V)	1.20
GRAVITY (g)	9.8 m s^{-2}
CORIOLIS PARAMETER (f)	0.0 s^{-1}
EDDY VISCOSITY (ν)	$1 \text{ m}^2 \text{ s}^{-1}$
EDDY CONDUCTIVITY (κ)	$10 \text{ m}^2 \text{ s}^{-1}$
PRANDTL NUMBER (P)	0.1
SEA SURFACE TEMPERATURE (T_{00})	300.5 K
TEMPERATURE AT $Z = h_{LB}$	25.4 °C
MIXING RATIO AT SEA SURFACE	22.33 g kg^{-1}
MIXING RATIO AT $Z = h_{LB}$	13.70 g kg^{-1}
RAYLEIGH NUMBER (Ra)	-1.0
SCHRAMM VELOCITY CONSTANT (s_m)	0.38
SCHRAMM THERMAL CONSTANT (s_T)	0.91

Because we expect the BLSE solutions to have time scales on the order of an hour or less, we neglect the Coriolis term in the model. In our model, we may specify only one wavenumber in each of the x - and y -directions, and so we set $l = 1$ and $m = 1$. The values chosen for κ and the Prandtl number P determine the value of the ν using (2.30). In this case, $\kappa = 10 \text{ m}^2 \text{ s}^{-1}$ and $P = 0.1$, which gives $\nu = 1 \text{ m}^2 \text{ s}^{-1}$.

For the next step in finding the physical parameter values, we determine the preferred values of the aspect ratios. The aspect ratios describe the horizontal domain shape by (2.30) and (2.31). In past studies of nonlinear dynamical system (NDS), the preferred aspect ratios have been found by performing eigensystem analyses for different values of the forcing represented by Ra or Re (e.g., Shirer 1986; Laufersweiler and Shirer 1989, 1995; Haack and Shirer 1992). The preferred aspect ratio values in those studies correspond to the pairs of aspect ratio values here, and their minimum Ra or Re values that are given by a conjugate pair of eigenvalues having zero real part in the linear stability analysis, corresponds to the minimum Re value here (Laufersweiler 1987). This result signals a Hopf bifurcation producing a periodic solution that, if supercritical and hence stable, is realized after the system transients have disappeared (e.g. Pyle 1987).

Figure 3.3 is a typical example of a plot used to determine the preferred values of the aspect ratios. The curve represents the vanishing of the greatest real part among the eigenvalues. The lowest point on this curve, giving the minimum critical Ra or Re and the preferred aspect ratio, can be found approximately by varying the aspect ratios in an eigensystem analysis for fixed values of Ra and Re . The aspect ratios that produce the largest positive real part in the eigenvalues for this fixed Ra and Re correspond to a point approximately above the preferred aspect ratio. As Ra or Re is varied to make the greatest real part tend towards zero, the corresponding aspect ratio approaches the preferred value.

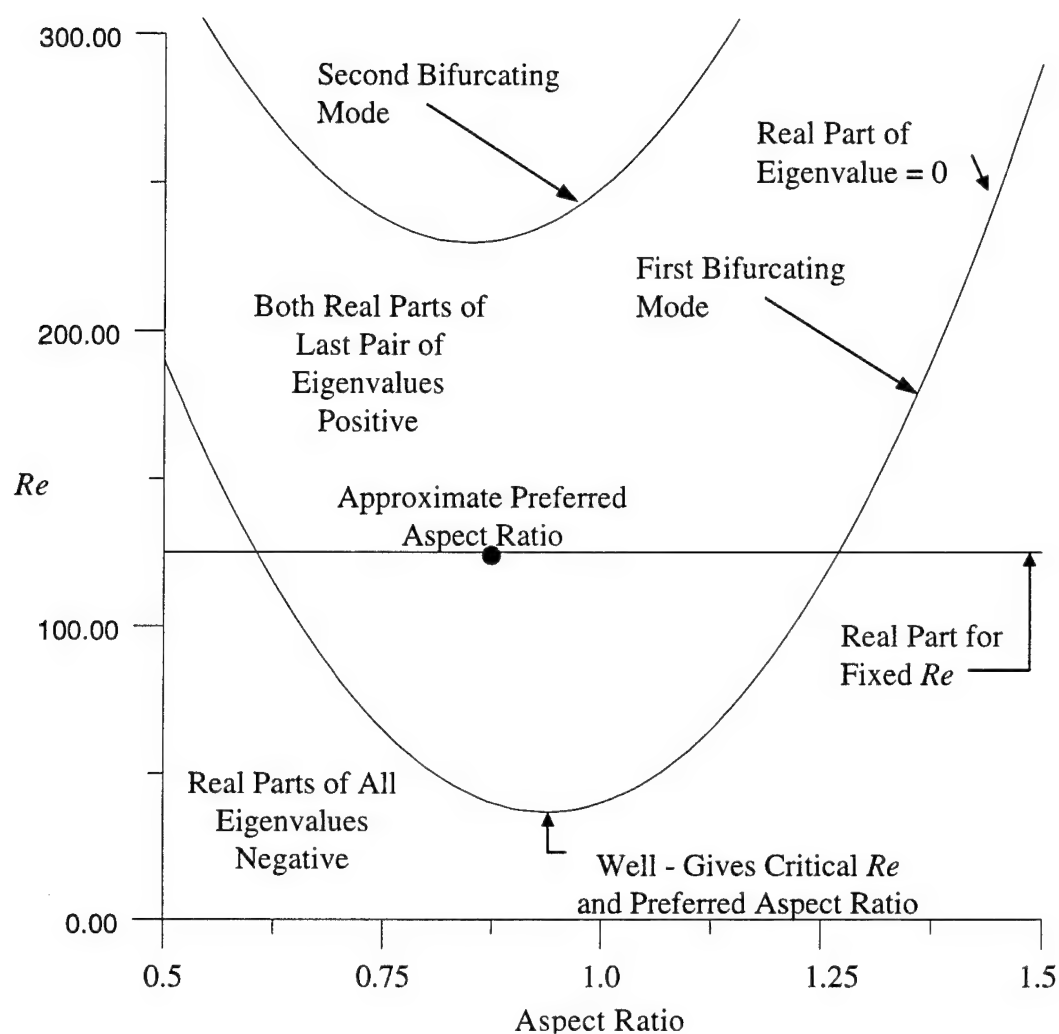


Fig. 3.3. Schematic plot of Re versus one aspect ratio while the other aspect ratio is fixed and $Ra = -1$.

The lower curve represents the vanishing of the real part of the eigenvalue having the largest real part. The real part of this last eigenvalue is negative below the curve and positive above it. The straight line is given by the value of Re used in a linear analysis. The approximate preferred aspect ratio can be found numerically by determining the largest real part along this line. This point represents the greatest distance from the line to the zero curve and therefore is above the well. As Re is varied to make the largest real part tend toward zero, the approximate preferred aspect ratio approaches the true preferred aspect ratio. A second pair of eigenvalues has positive real part above the curve for the second bifurcating mode. The $Re = \text{constant}$ line is chosen below this second curve.

However in our NDS we have separated the thermal forcing at the lower boundary from the thermal forcing within the boundary layer. The Ra value in our NDS controls the thermal forcing within the boundary layer and s_T controls the thermal forcing at the lower boundary. The observed meteorological conditions determine the value of s_T . We choose a thermally neutral atmosphere for this case study, so $Ra = -1$ according to the energetics analysis discussed in Chapter 2 and Appendix A.

Since we have constant s_T , s_m , and Ra , but an unknown wind profile, we determine the preferred values of the aspect ratios by using a critical Re , instead of a critical Ra , in our eigensystem analyses. For a given Re , we perform a linear eigensystem analysis as we loop through the aspect ratios — a_x and a_y . Since the Hi-Res case study is a light-wind case, we choose an appropriate initial Reynolds Number $Re = 250$; this corresponds to wind speeds, relative to the ocean current, of 1.95 m/s at $z_{hlb} = 10 \text{ m}$ to 2.81 m/s at $z_T = 900 \text{ m}$. Figure 3.4 is a plot of the results for this linear analysis. The plot shows the real part of the last eigenvalue (eigenvalues ordered with respect to the real part) from the analysis for each aspect ratio set, which as we note above gives the preferred values. From the plots, we look for the largest positive values contoured toward a ringed maximum. Figure 3.4 displays an obvious contoured maximum. We perform another linear analysis around this maximum using a finer resolution loop of the aspect ratios. From this refined analysis, we determine the aspect ratios at the maximum point. For this case study, we then look at a similar plot for the next pair of eigenvalues up in the list to ensure that there is not another bifurcating mode indicated for the above set of preferred aspect ratios and Re value. If there is another bifurcating solution, then we decrease the Re until we isolate a set of preferred aspect ratios with only one bifurcating solution (Fig. 3.3). The final set of aspect ratios for the smallest maximum real parts

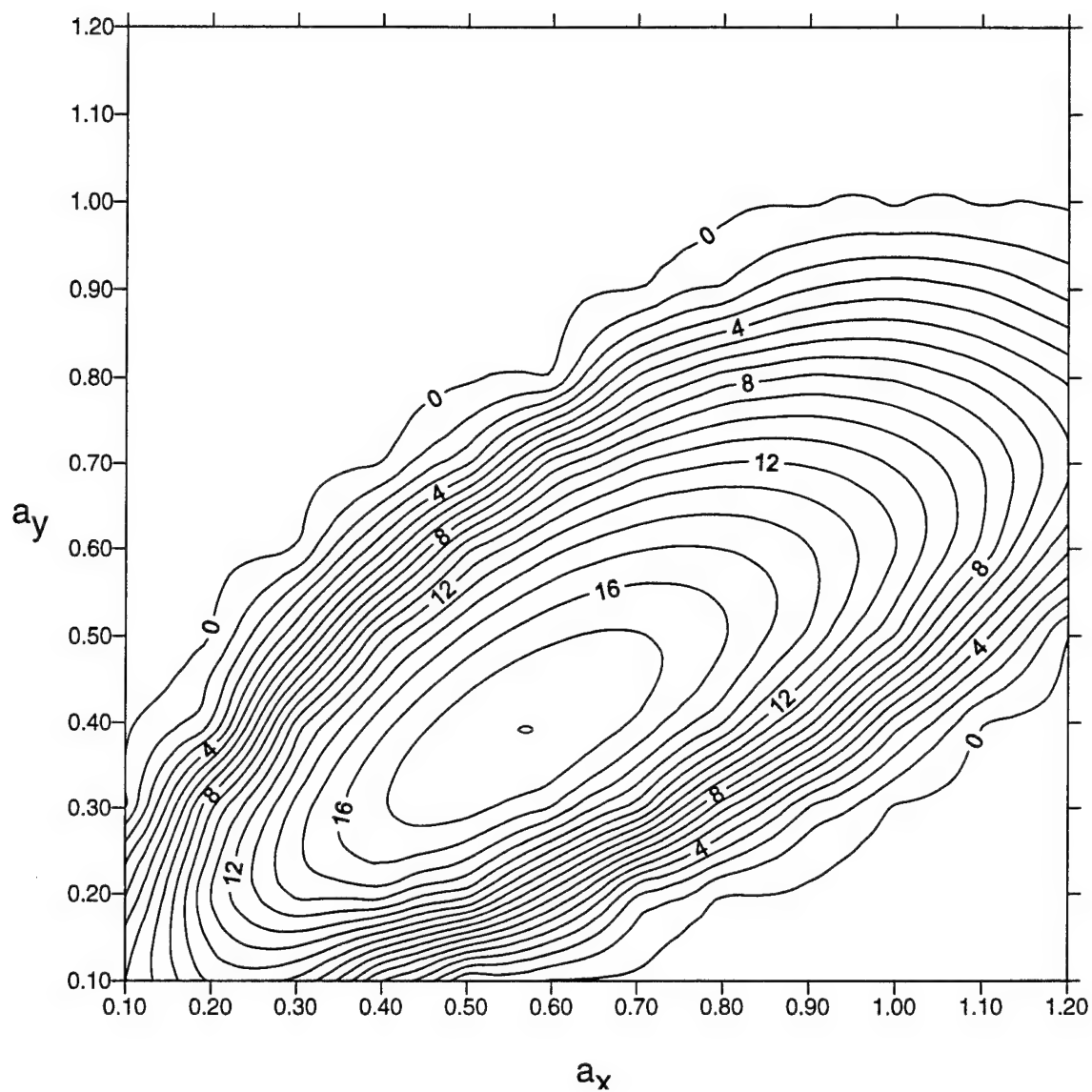


Fig. 3.4. Contour plot of the real part of the last eigenvalue from the linear eigensystem analysis for $Re = 250$. The maximum value indicates the preferred aspect ratios for the BLSE modes.

together with the Re value are chosen for use in our case study. The analyses yielded a Reynolds number: $Re = 250$, preferred aspect ratios: $a_x = 0.56$ and $a_y = 0.38$ and only one bifurcating solution. Now that we found a Re value, we can plot the mean current-relative wind profile, Fig. 3.5.

We determine the initial conditions by using the eigensystem analysis. We find the real (or imaginary) parts of the eigenvector associated with the preferred aspect ratios and eigenvalue found above. These values tell us the approximate relative magnitudes of the coefficients in the nonlinear branching solution.

As noted in Chapter 2, the IMSL integration routine uses the Adams-Gear method. We perform a series of model integrations to determine the proper value for the time step. The time step is reduced until the number of internal subroutine calls is small enough to allow accurate solutions at each step. We find the largest possible time step to be 1 second. Next, we run the model integration for a number of hours, to allow sufficient time for the system to equilibrate. We determine when the system reaches a quasi-equilibrated state by plotting the square root of the sum of the squares of the 50 time-dependent amplitude coefficients.

Starting with the original eigenvector, the model integration took 18 hours (32,400 time units) to equilibrate. A plot of the square root of the sum of the squares is given in Fig. 3.6. If we had multiplied the eigenvector by a constant to obtain values on the scale of the model amplitude coefficients, and then had used the resulting values as initial conditions, then we believe that the model might have equilibrated faster. The constancy of the energy after equilibration matches results acquired by Shirer (1986), Pyle (1987), and Haack and Shirer (1992).

We also check the validity of the model by examining the periodicity of the solution. Using a linear eigensystem analysis, we determine the values for the imaginary

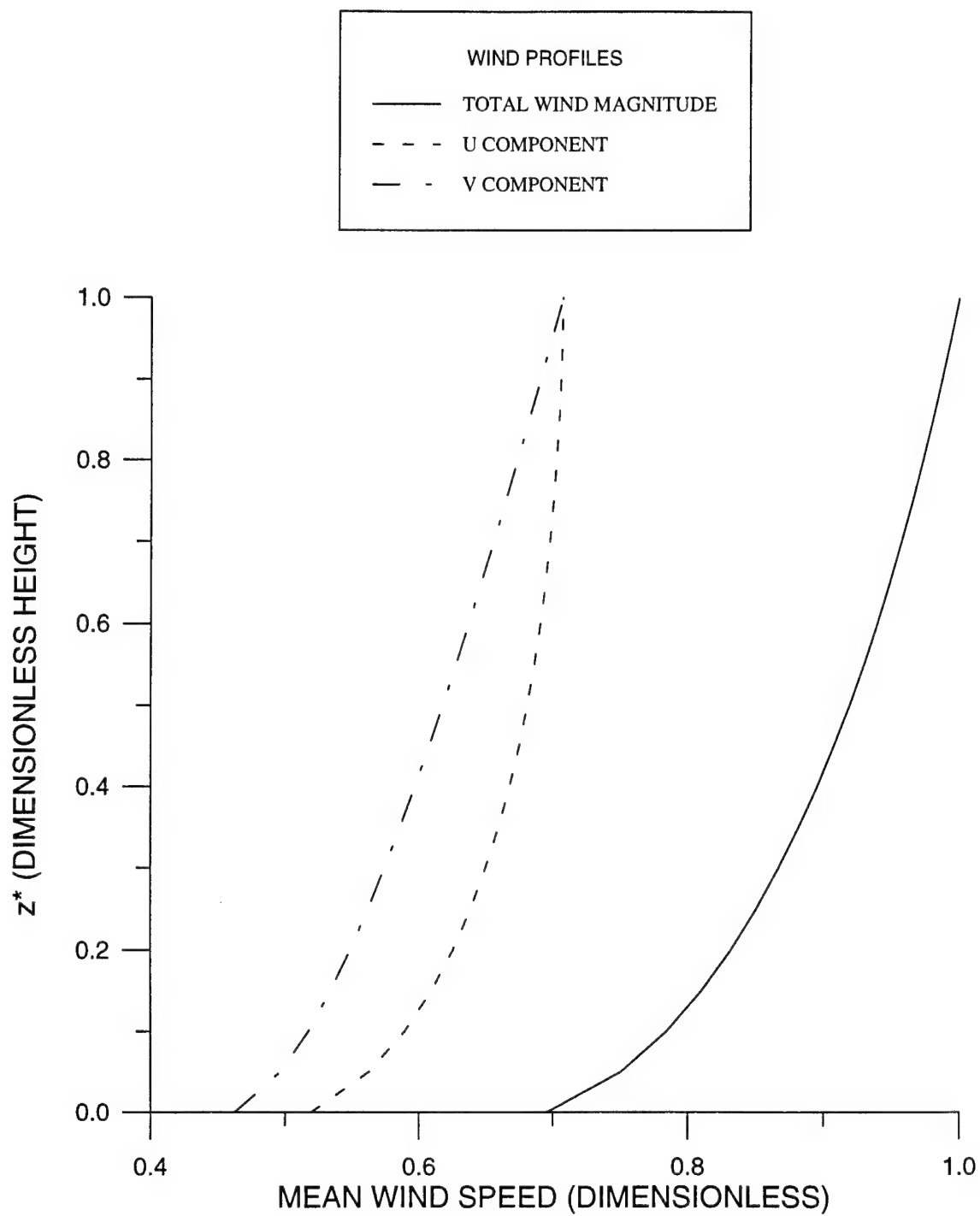


Fig. 3.5. Mean current-relative wind profile with predominantly speed shear that is used in case study.

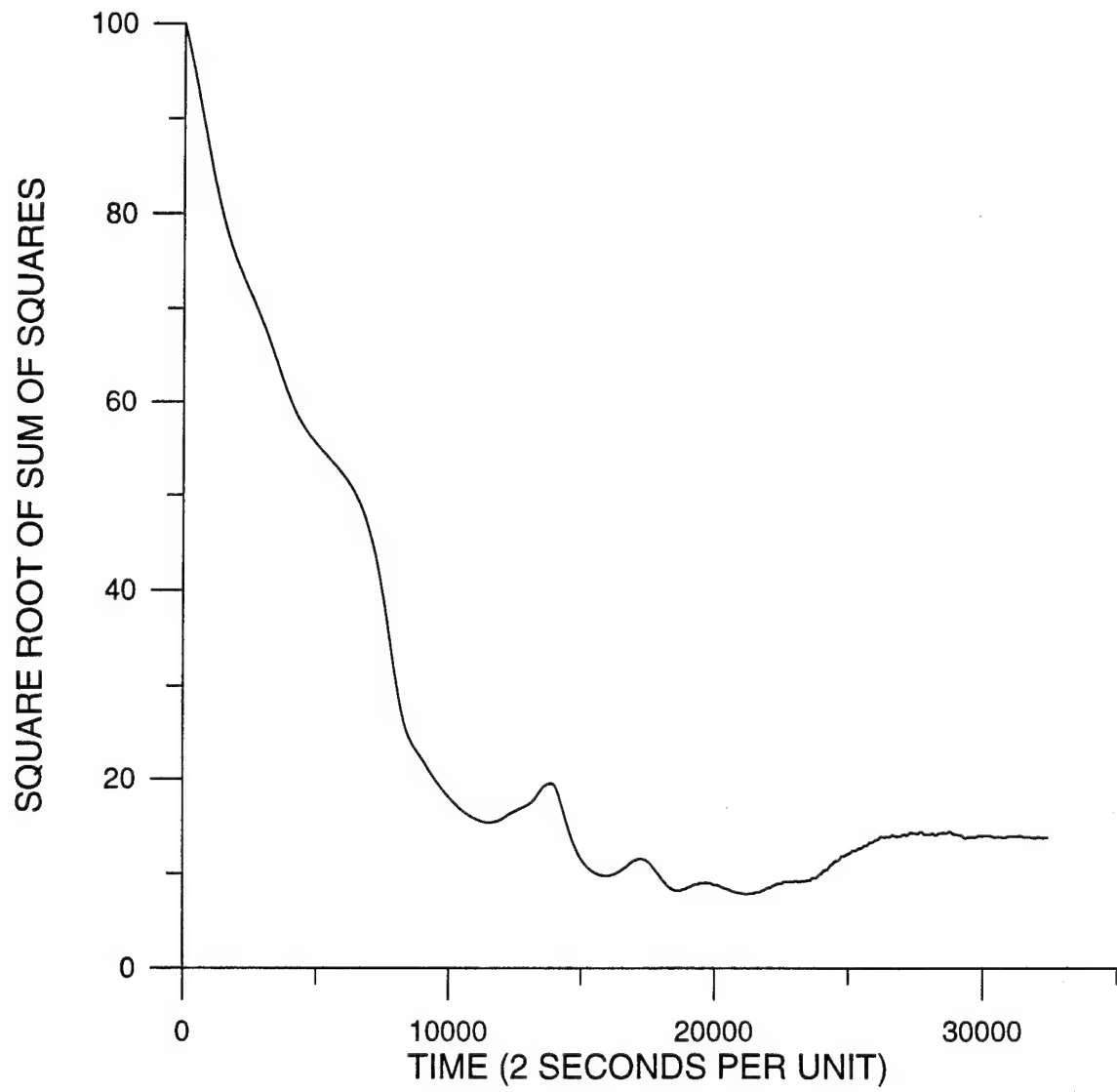


Fig. 3.6. The square root of the sum of the squares for the 50 time-dependent amplitude coefficients.

parts Im of the eigenvalues. We calculate the limiting period of the bifurcating solution, using the Im for the last eigenvalue, by (Pyle 1987),

$$Period = \frac{2\pi}{Im}. \quad (3.5)$$

This value must then be converted to dimensional units using (2.19). Based on our analysis, $Im = 229.5$. Using the above equation, we find a dimensionless period of 2.738×10^{-2} , or 36.22 minutes.

Given our small-speed-shear wind profile, this period should correspond to the speed of movement of the cells caused by advection by the mean wind. To find this speed, we first note that the ratio $L_y/L_x = a_x/a_y$ serves as a measure of the orientation angle θ of a BLSE axis, for which $\tan\theta = a_x/a_y$; here θ is the angle between the BLSE axis and east. At any level, the background wind angle ϕ is given by $\tan\phi = V/U = V^*/U^*$. Thus it follows that the angle $\phi - \theta$ between the background wind vector and the BLSE axis obeys (Zuccarello 1994)

$$\tan(\phi - \theta) = \frac{\tan\phi - \tan\theta}{1 + \tan\phi \tan\theta} = \frac{a_y V^* - a_x U^*}{a_y U^* + a_x V^*}. \quad (3.6)$$

For the case discussed here, $a_x = 0.56$ and $a_y = 0.38$, angle θ of the BLSE axis is 56° (north of east), and so, with the layer mean values $\bar{U} = 1.98 \text{ ms}^{-1}$, $\bar{V} = 1.70 \text{ ms}^{-1}$, and $|\bar{V}| = 2.61 \text{ ms}^{-1}$, the angle $\phi - \theta$ between the wind direction and the BLSE-axis is approximately 14° . The component \tilde{U} along the BLSE axis is given by

$$\tilde{U} = \bar{U} \cos\theta + \bar{V} \sin\theta, \quad (3.7)$$

and \tilde{V} across this axis is given by

$$\tilde{V} = -\bar{U} \sin\theta + \bar{V} \cos\theta . \quad (3.8)$$

These components introduce advection periods equal to L/\tilde{V} and L/\tilde{U} , where L is the BLSE axis $L = (z_T - h_{LB})/\sqrt{a_x^2 + a_y^2}$. Here L is approximately 1330 m; which produces periods of 35.11 minutes and 8.8 minutes, respectively. The first period is close to the value of 36.22 minutes given by (3.5). These periods are under an hour and so are consistent with our neglecting of the Coriolis term.

We next check these estimates for the periods against the nonlinear results for one of the time-dependent amplitude coefficients T_{11} given by the numerical integration. The periods seen in the graph in Figs. 3.7 are approximately 36 minutes and 9 minutes, therefore demonstrating that the model integration is accurately reproducing the expected periodicities of the solution. The other BLSE coefficients also have periods of approximately 36 minutes and 9 minutes, while the BLSE modification terms become steady. These results are also consistent with the results of Shirer (1986), Pyle (1987), and Haack and Shirer (1992).

3.3. BLSE Patterns

We use the physical parameter values in Section 3.2 to examine the chosen case of BLSE for the time of the SAR image. Our goal is to determine whether the model might

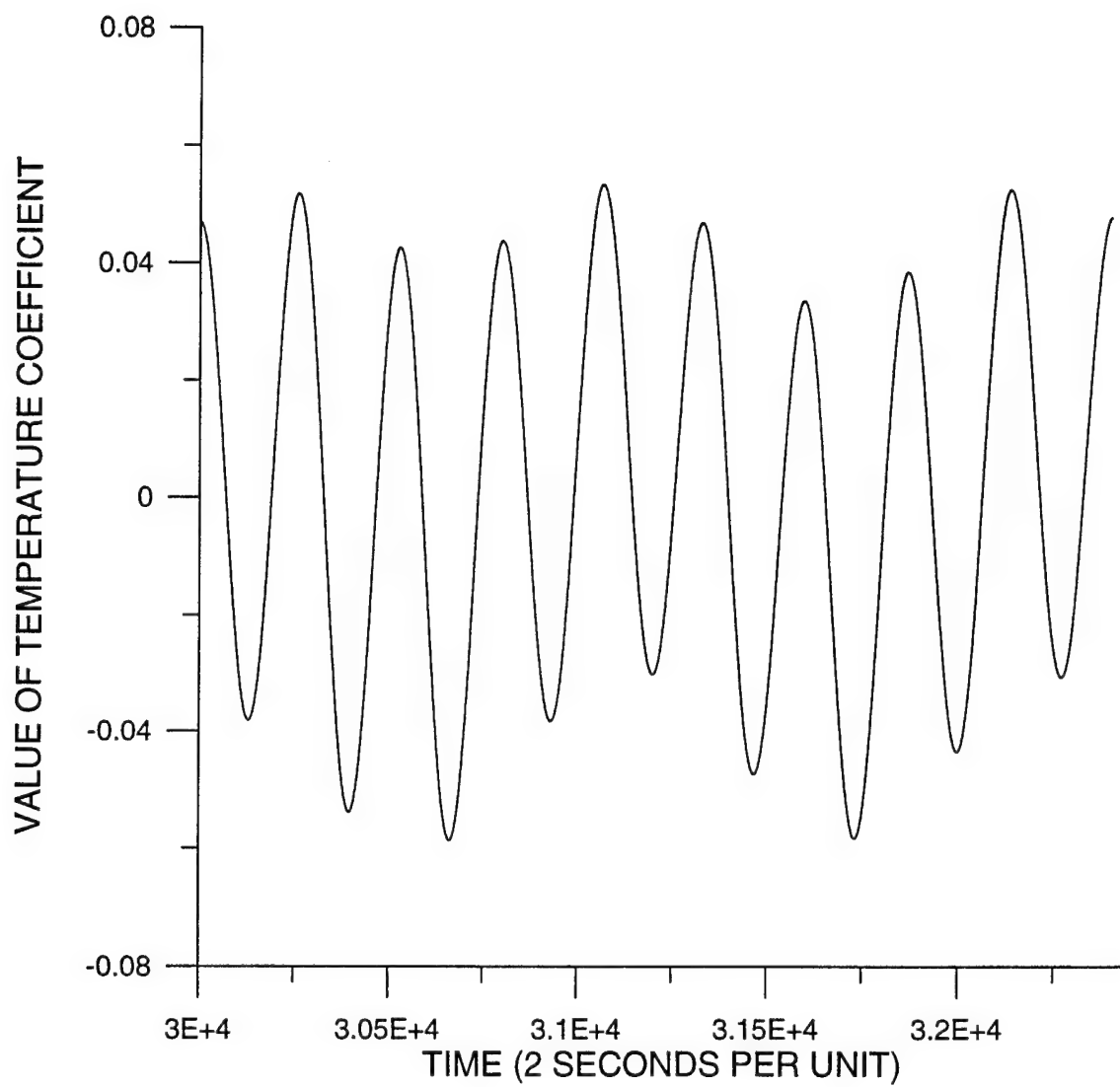


Fig. 3.7. Time series of one of the time-dependent temperature amplitude coefficients (T_{11}), demonstrating that the bifurcating solution has periods of approximately 36 minutes and 9 minutes.

explain the patterns seen in the SAR image and to verify that the new boundary conditions produce the expected behavior in the various physical quantities. We analyze and compare profiles and cross-sections with results from other models, and then we compare planview patterns from the model with those we find on the SAR image.

Our first step is to determine whether the model captures the proper spatial organization. One way of examining this structure is to analyze the vertical cross-section of the domain along the two axes: x^* -along, given by

$$\tilde{x}^* = x^* \cos\theta + y^* \sin\theta , \quad (3.9)$$

and \tilde{y}^* -across, given by

$$\tilde{y}^* = -x^* \sin\theta + y^* \cos\theta . \quad (3.10)$$

These axes depend on the orientation angle $\theta = \tan^{-1}(a_x/a_y)$, and they are approximately along and perpendicular to the mean wind direction, respectively. Then we rotate the wind components and streamfunctions via

$$\tilde{u}^* = u^* \cos\theta + v^* \sin\theta . \quad (3.11)$$

$$\tilde{v}^* = -u^* \sin\theta + v^* \cos\theta . \quad (3.12)$$

$$\tilde{\psi}^* = \psi^* \cos\theta - \eta^* \sin\theta \quad (3.13)$$

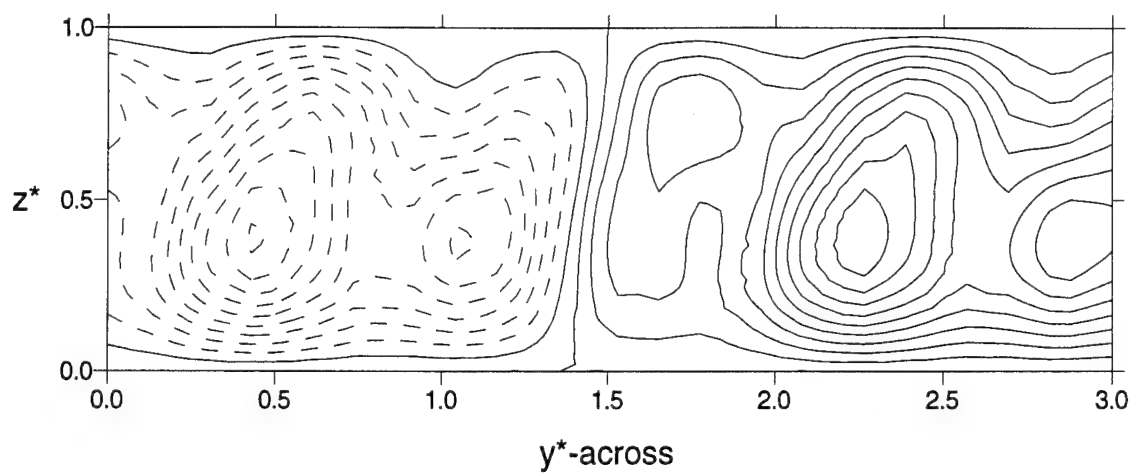
$$\tilde{\eta}^* = \psi^* \sin\theta + \eta^* \cos\theta . \quad (3.14)$$

This rotation does produce cross-sections exhibiting simple horizontal periodicity. We present the contoured streamfunctions $\tilde{\psi}^*$ and $\tilde{\eta}^*$ in the cross-wind direction \tilde{y}^* in Fig.

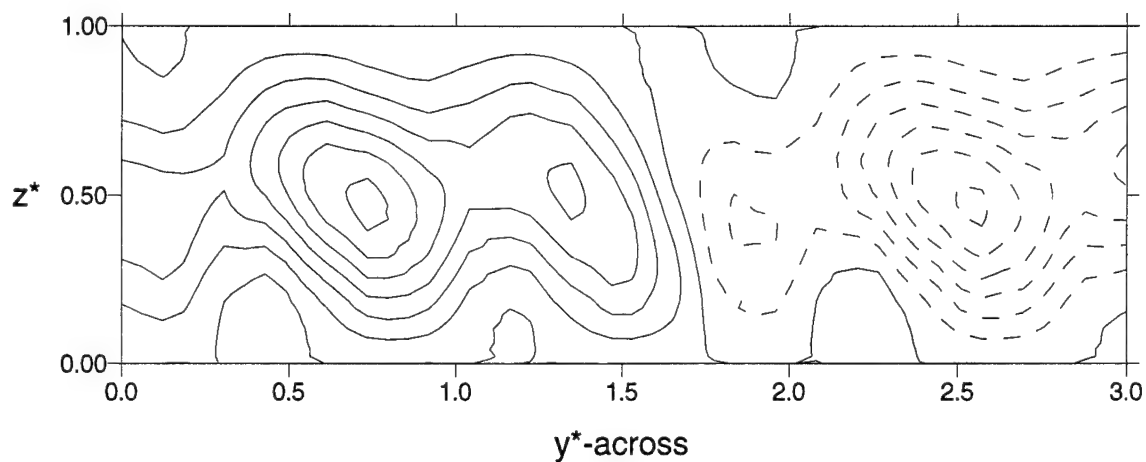
3.8(a) and Fig. 3.8(b), and in the along-wind direction \tilde{x}^* in Fig. 3.9(a) and Fig. 3.9(b). We immediately see that the BLSE are three-dimensional as predicted from the data on the Woodcock diagram (Fig. 3.2). In addition, the circulations fill the entire vertical domain. It is thus clear that vertical wavenumber one is dominant, but there is also evidence of the other vertical wavenumbers. The horizontal trigonometric functions are interacting, as seen by the lateral nonsymmetry. As noted above, the approximately repeating horizontal pattern is due to our axis rotation by the orientation angle θ . In the $\tilde{\psi}^*$ diagrams (part (a) in both figures), we observe large horizontal components along the lower boundary that contribute to the downward transfer of momentum and therefore to the sea-surface stress. However, this pattern in $\tilde{\psi}^*$ may oscillate between $\tilde{\psi}^*$ and $\tilde{\eta}^*$ throughout a period, and this possibility will be explored later.

In Fig. 3.10(a) and Fig. 3.10(b), we look at the cross-section perturbation temperature contours using the same rotated axes. In these figures, we find that the temperature exhibits a vertical wavenumber two pattern in both cross-sections. Both this pattern and the streamfunction patterns are similar to Schmidt and Schumann's (1989) temperature and streamfunction patterns produced by their large-eddy simulation (LES). Their LES run had an inversion, while our NDS does not have an inversion; thus the similarity in the cross-sections is quite gratifying.

To complement the contoured streamfunction diagrams, we examine the domain cross-section velocity vectors whose horizontal components are \tilde{u}^* and \tilde{v}^* . Here, the perturbation velocity \tilde{u}^* is given by the curl of the streamfunction $\tilde{\eta}^*$ and the perturbation velocity \tilde{v}^* is given by the curl of the streamfunction $\tilde{\psi}^*$. Figures 3.11(a) and 3.11(b)

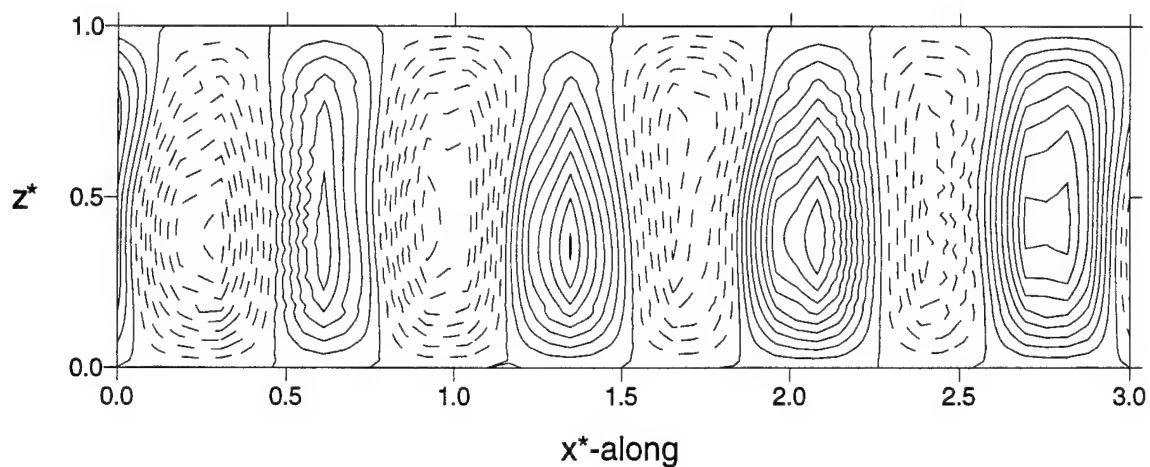


(a)

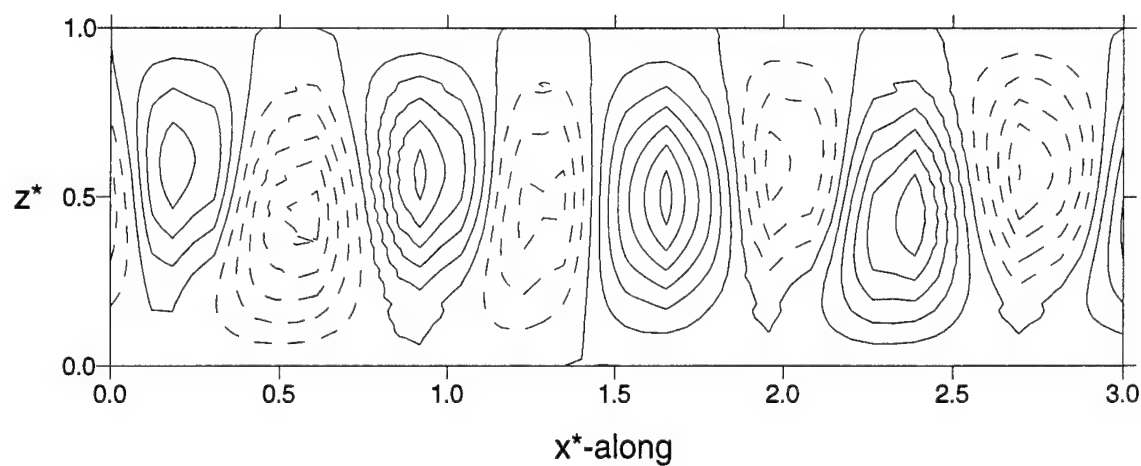


(b)

Fig. 3.8. Domain cross-section of contoured streamfunctions: (a) ψ^* and (b) η^* in the cross-mean-wind direction \bar{y}^* -across. The η^* contours represent \bar{u}^* approximately along the mean wind direction and the ψ^* contours represent \bar{v}^* approximately perpendicular to the mean wind direction. The solid contours are positive values and the dashed contours are negative values.

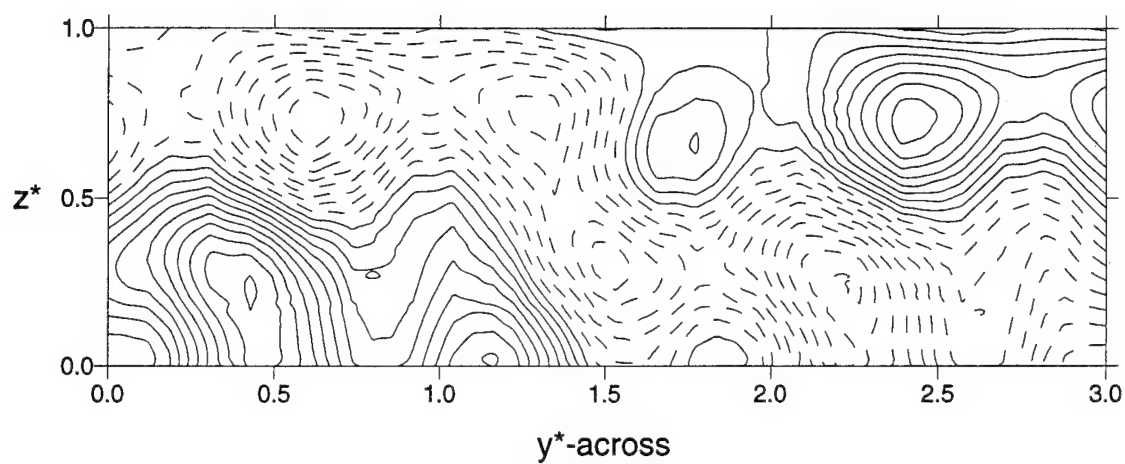


(a)

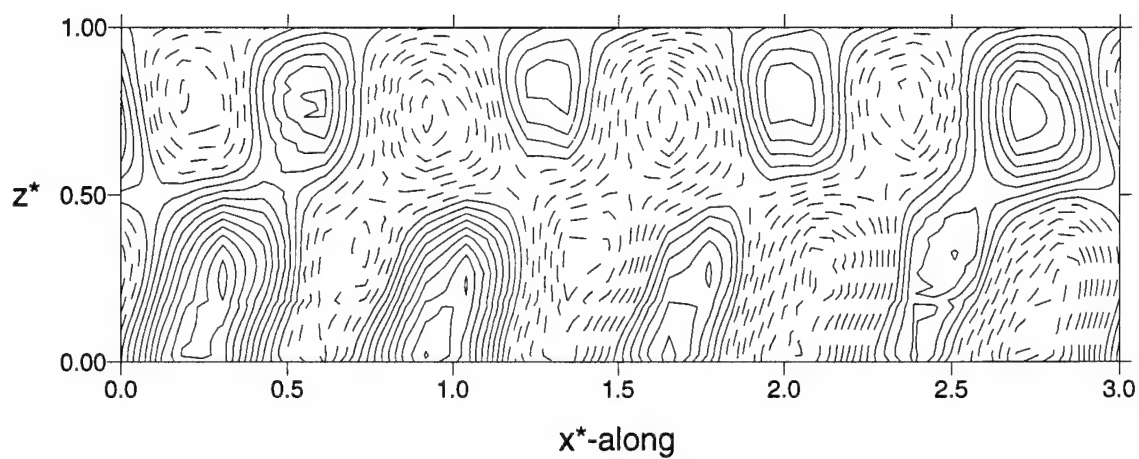


(b)

Fig. 3.9. Domain cross-section of contoured streamfunctions: (a) $\tilde{\psi}^*$ and (b) $\tilde{\eta}^*$ in the along-mean-wind direction \tilde{x}^* -along. The $\tilde{\eta}^*$ contours represent \tilde{u}^* approximately along the mean wind direction and the $\tilde{\psi}^*$ contours represent \tilde{v}^* approximately perpendicular to the mean wind direction. The solid contours are positive values and the dashed contours are negative values.

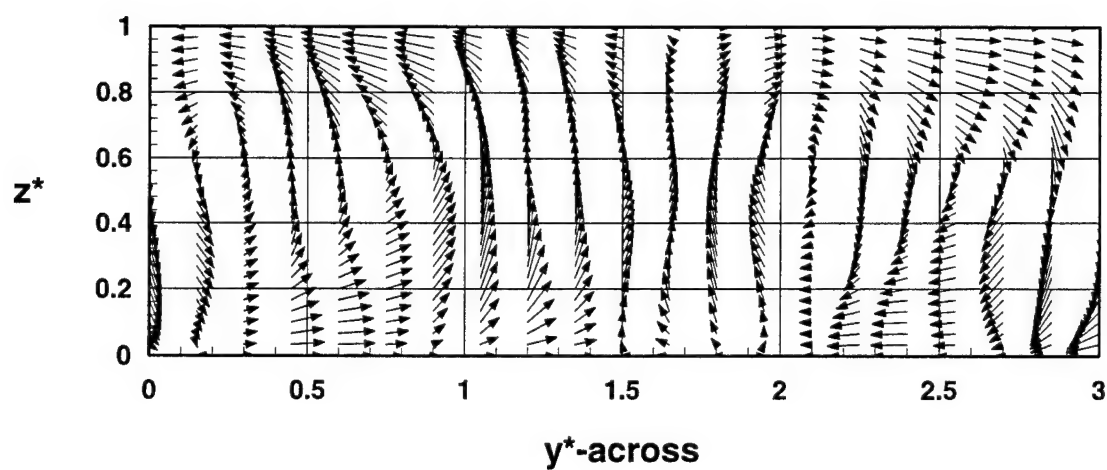


(a)

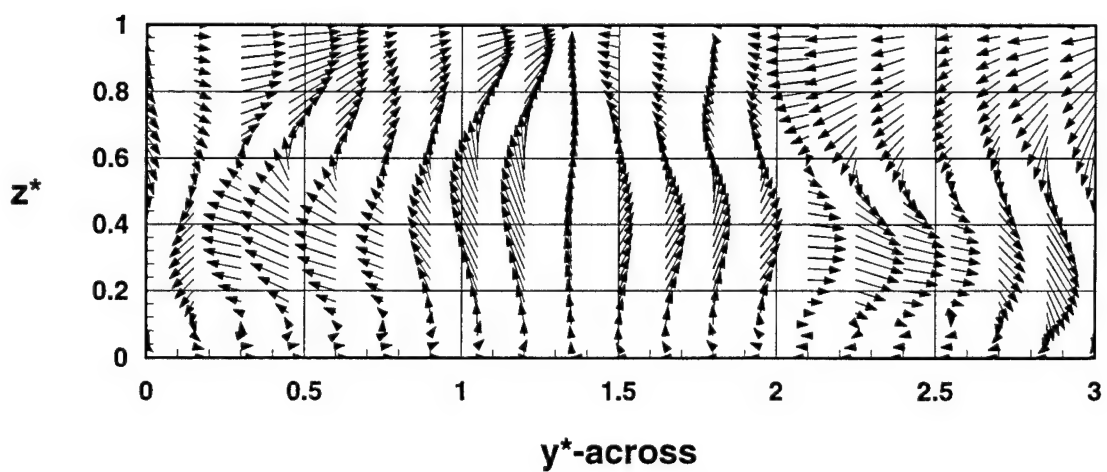


(b)

Fig. 3.10. Domain cross-section of contoured temperature : (a) across-mean-wind direction \bar{y}^* -across and (b) along-mean-wind direction x^* -along. The solid contours are positive values and the dashed contours are negative values.



(a)



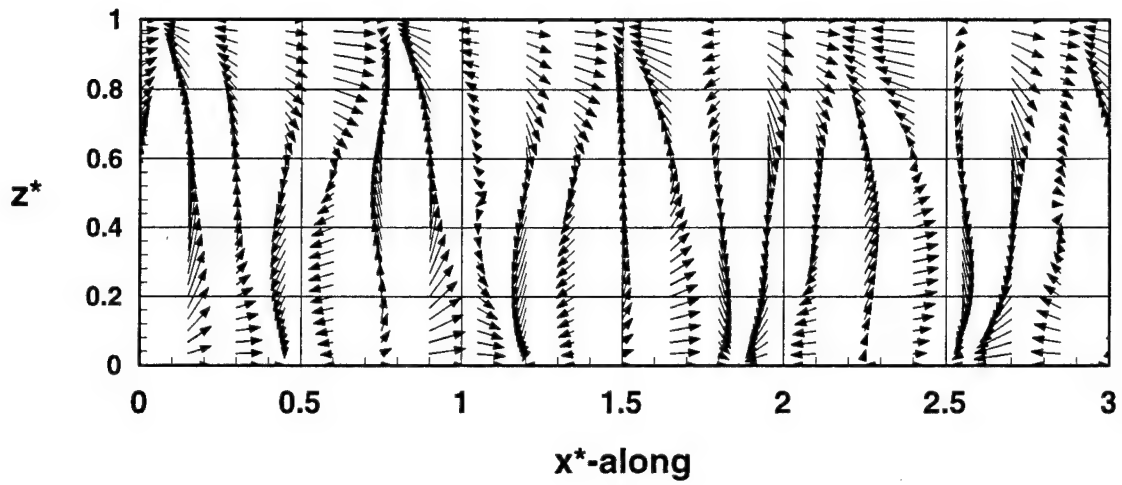
(b)

Fig. 3.11. Domain cross-section of velocity vectors: (a) (\tilde{v}^*, w^*) and (b) (\tilde{u}^*, w^*) in the cross-mean-wind direction \tilde{y}^* -across.

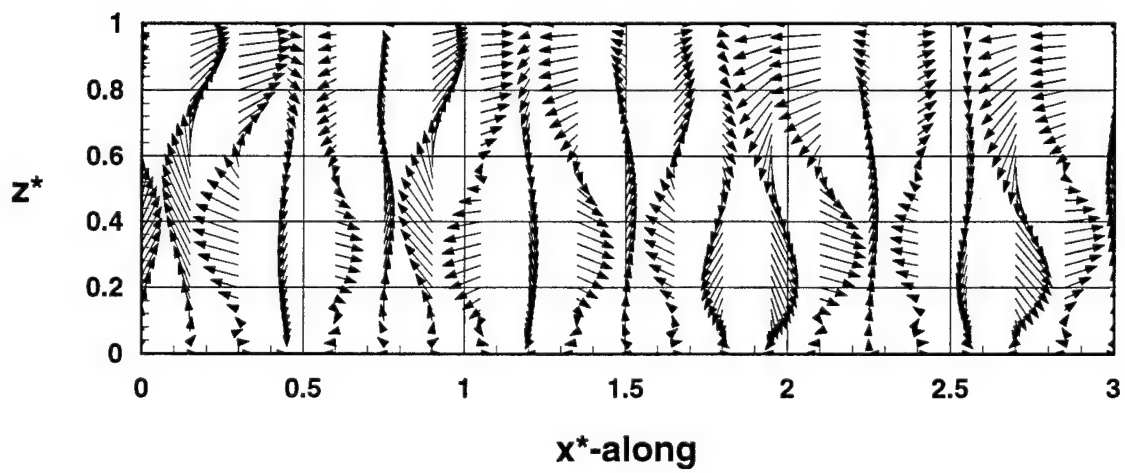
present the (\tilde{v}^*, w^*) and (\tilde{u}^*, w^*) velocity vector fields in the cross-wind direction and correspond to the streamfunctions in Fig. 3.8(a) and Fig. 3.8(b), respectively. Figures 3.12(a) and 3.12(b) present the (\tilde{v}^*, w^*) and (\tilde{u}^*, w^*) velocity vectors in the along-wind direction and correspond to the streamfunctions in Fig. 3.9(a) and Fig. 3.9(b), respectively. In these figures, we see that areas of divergence and convergence are offset in the vertical suggesting a tilt to the circulation. We also find interesting small-scale circulations near the lower boundary in Fig. 3.11(b). These circulations are responsible for some downward transport of momentum to the sea-surface.

The velocity vector cross-sections display numerous strong updrafts and downdrafts. We next examine the dimensional vertical velocity profile for the center of an updraft in Fig. 3.13. This graph indicates that in the updraft, the maximum vertical velocity occurs at $z^* = 0.35$ and has a typical magnitude. This result shows that by controlling the vertical velocity at the lower boundary, we force the maximum vertical velocity up into the middle of the boundary layer where it actually occurs. This result is consistent with convective boundary layer observations (*e.g.*, Lenschow *et al.* 1980) and other model simulations. Therefore, we have solved Zuccarello's (1994) second problem with the model.

The model-calculated winds affect the mean wind profile. The unrotated, dimensional, horizontally-independent wind profile components, u -modification given by η_{0q} and v -modification given by ψ_{0q} , are plotted in Fig. 3.14 and Fig. 3.15. These steady profiles are independent of the horizontal position in the domain and have a sensible magnitude. Both profiles show that the BLSE circulation is redistributing the shear in the background wind (Haack and Shirer, 1992).



(a)



(b)

Fig. 3.12. Domain cross-section of velocity vectors: (a) (\tilde{v}^*, w^*) and (b) (\tilde{u}^*, w^*) in the along-mean-wind direction \tilde{x}^* -along.

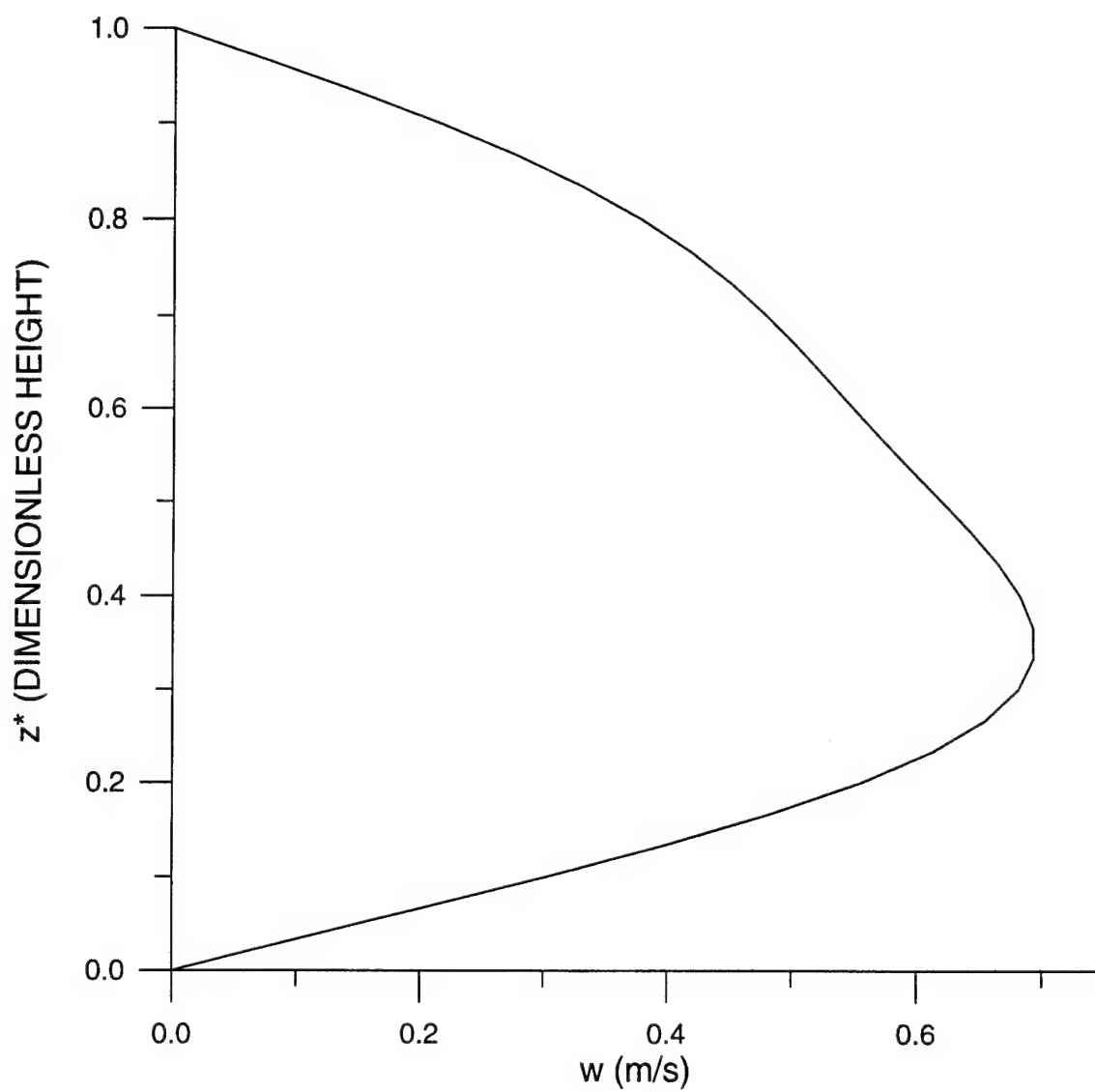


Fig. 3.13. Dimensional vertical velocity profile for the center of an updraft.

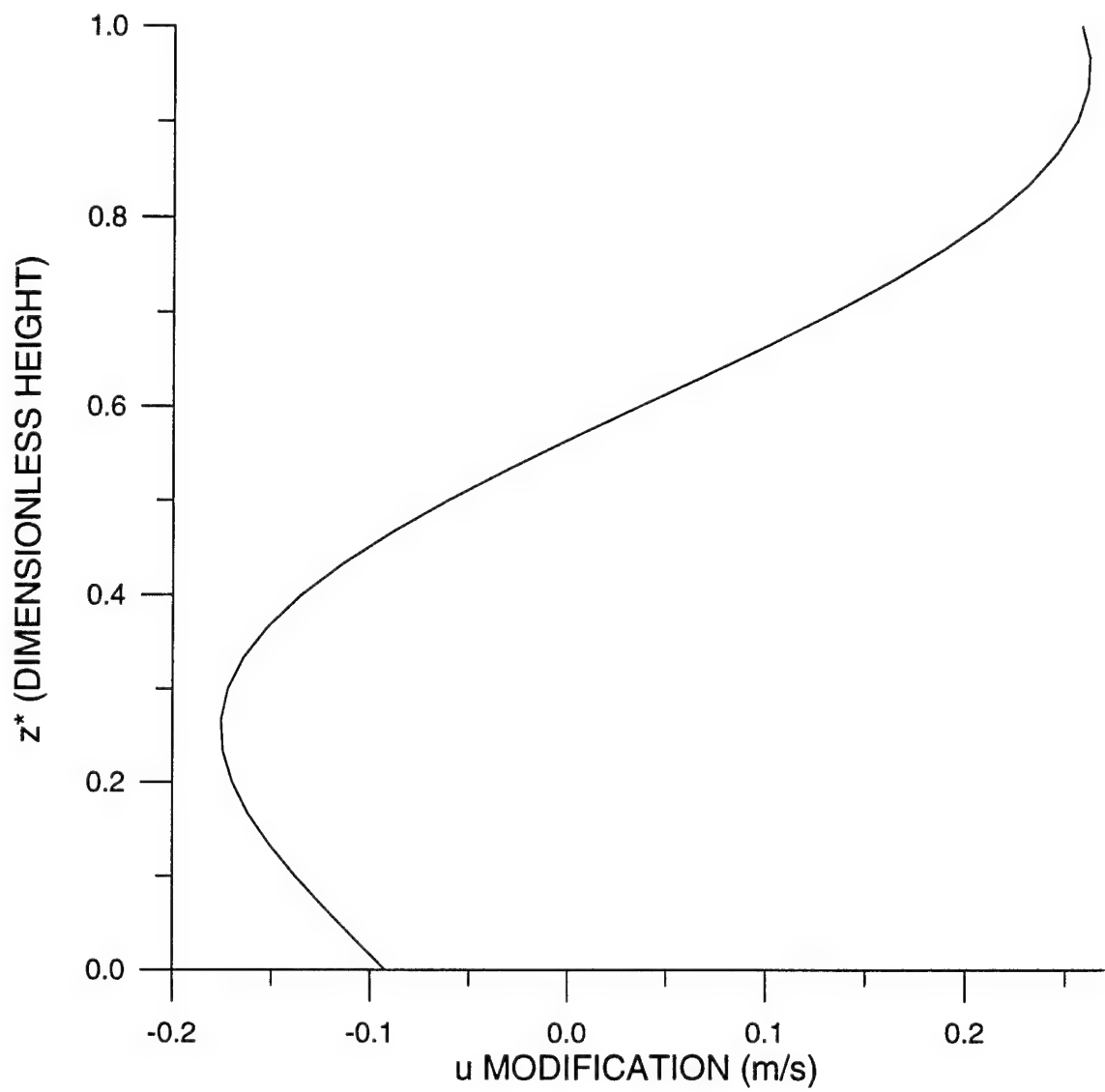


Fig. 3.14. Vertical profile of the dimensional wind modification velocity components given by η_{0g} .

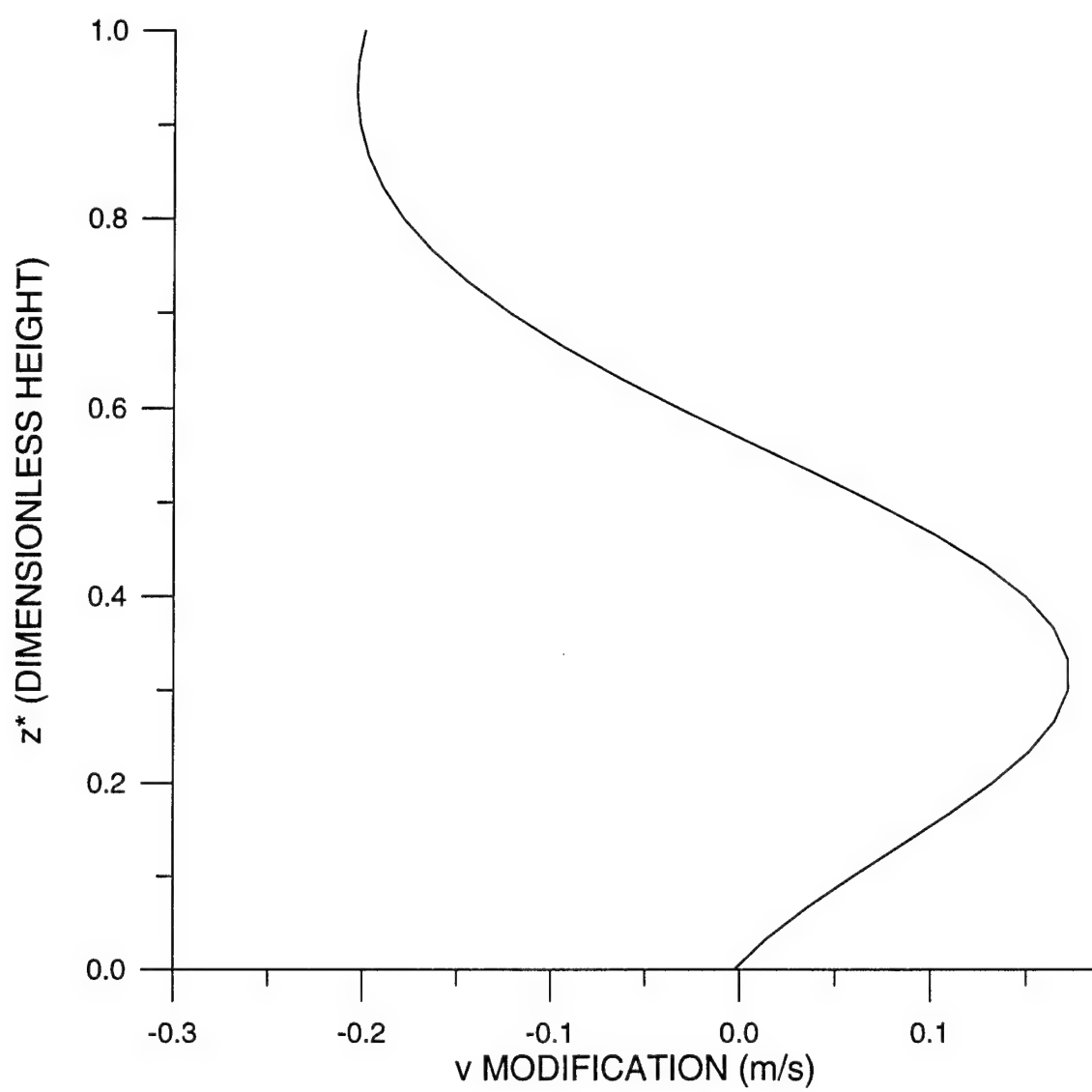


Fig. 3.15. Vertical profile of the dimensional wind modification velocity components given by ψ_{0g} .

The temperature profile modification by the circulation, given by T_{0q} , is shown in Fig. 3.16. This steady profile is again independent of location in the horizontal. The linear profile makes sense, as we have heating only from below and a thermally neutral atmosphere, given by $Ra = -1$. This plot helps justify the constant Ra approach of Haack and Shirer (1992) and others. The higher temperature at the lower boundary is consistent with the upward heat flux prescribed by $s_T > 0$ in our boundary conditions (Fig. 2.1).

In the next step we determine whether the model captures the observed kilometer-scale stress patterns seen in the SAR image of Sikora *et al.* (1995). We first examine the complete model-calculated velocity field at the lower boundary in Fig. 3.17. This pattern is obtained from the vector sum of the circulation velocity vectors and the wind profile modification velocity vectors, which are expressed relative to the ocean current. The velocity field displays a distinct three-dimensional cellular pattern, as expected from the above results, with a horizontal spacing of 1330 m. The prominent orientation of the lines of cells is transverse to the background wind, and, from the θ value above, is 34° west of north. The shape of the domain is chosen to match the dimensions given by the preferred aspect ratios for easy comparison with the SAR image.

By similarity theory, the horizontal velocity at the lower boundary is proportional to the horizontal velocity at the sea surface (*e.g.* Stull 1988). By the standard drag law parameterization, the total horizontal wind speed is proportional to the square-root of the sea-surface stress magnitude (*e.g.* Stull 1988). To find this magnitude, we therefore need the vector sum of the complete model-calculated winds and the background mean wind, which also is expressed relative to the ocean current. The resulting stress pattern is plotted in Fig. 3.18, with small values shaded more and large values shaded less in order to match the brightness of the stress pattern on the SAR image. Quite pleasingly, the

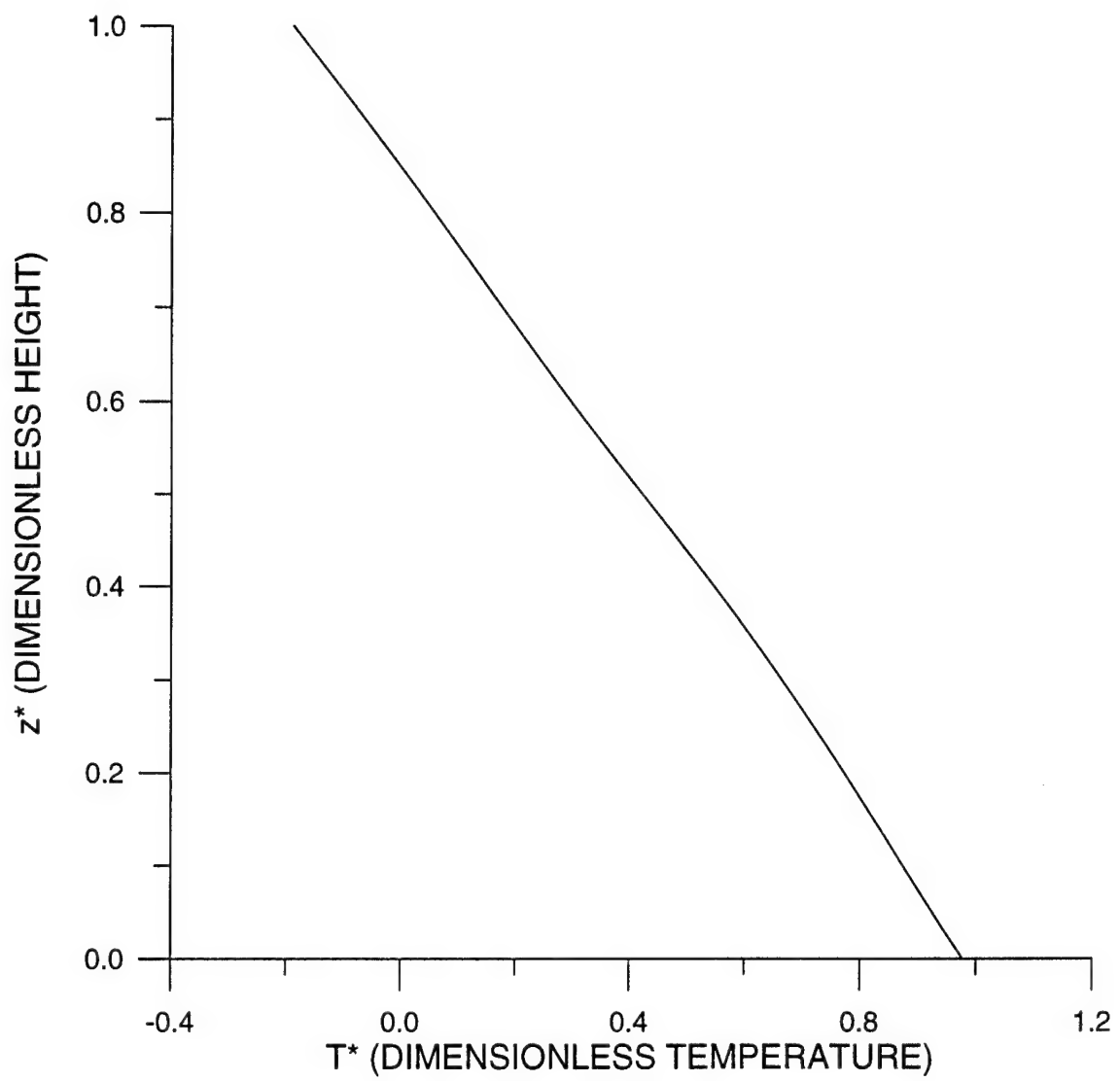


Fig. 3.16. Vertical profile of the dimensionless temperature modification given by T_{0q} .

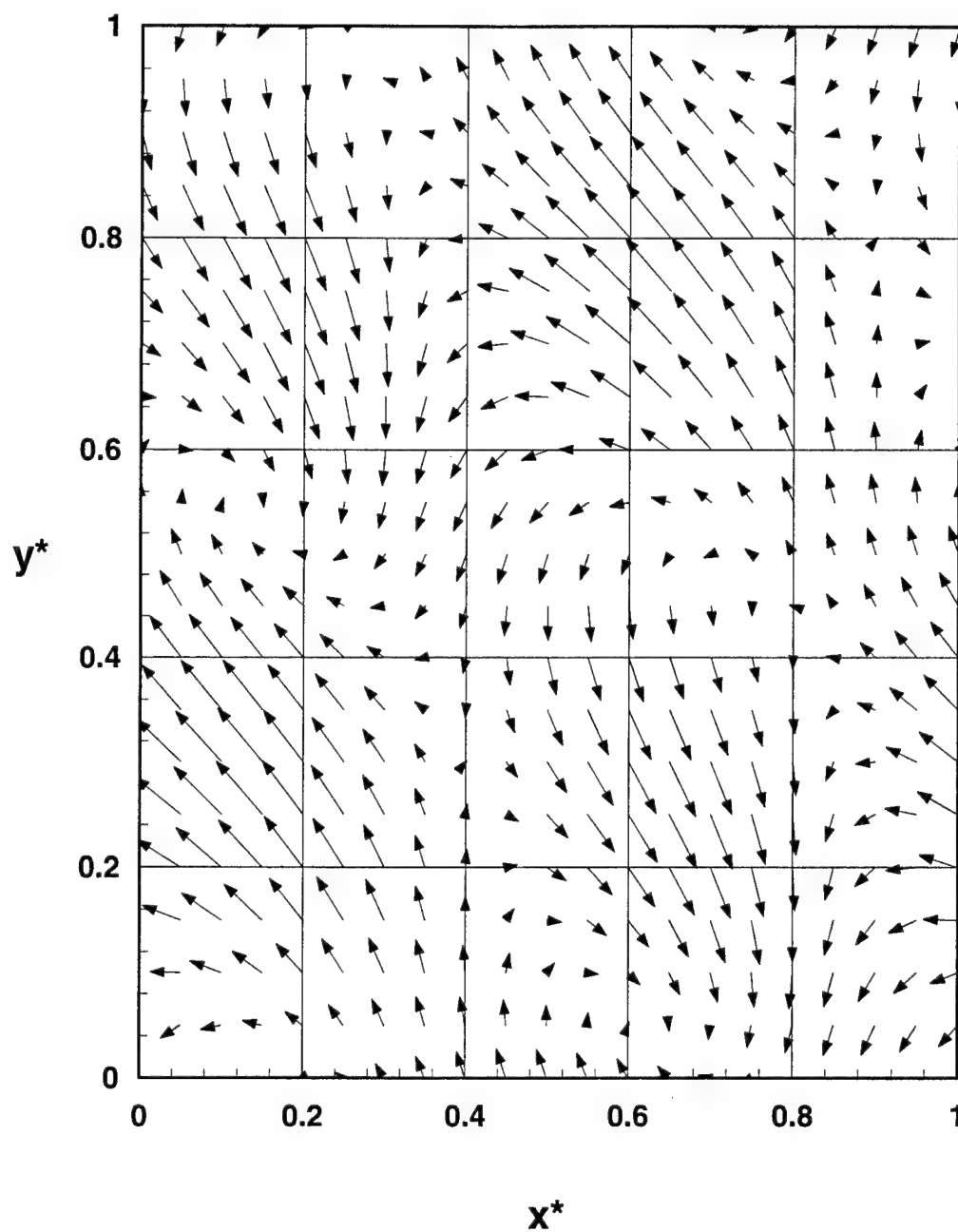


Fig. 3.17. Planview of complete horizontal dimensionless velocity field at the lower boundary $z^* = 0$.
The shape of the domain is chosen to agree with the ratio a_y/a_x , the actual slope of the \tilde{y} -axis.

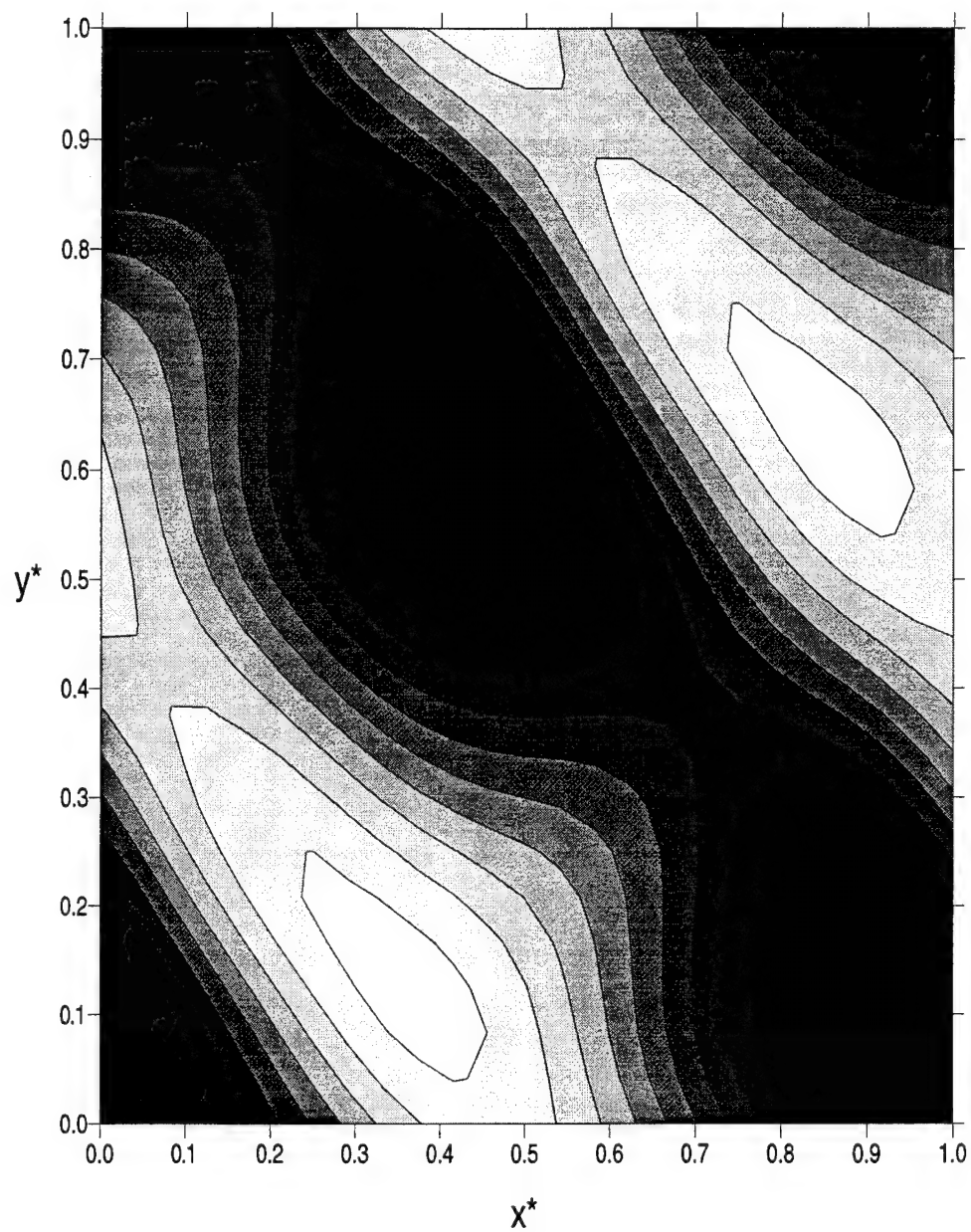


Fig. 3.18. Planview of stress magnitudes at the lower boundary $z^* = 0$. Small values are shaded more, large values are shaded less, in order to match the brightness of the stress pattern on the SAR image. The domain shape is chosen as in Fig. 3.17.

stress pattern on this planview matches fairly well the orientation of 35° west of north and the spacing of approximately 1000 *m* observed in the stress pattern in the SAR image published in Sikora *et al.* (1995).

3.4 Case Study Conclusions

We are quite pleased with the way the model is now running. The energetics analysis and the incorporation of the new boundary conditions enabled us to identify and correct some coding errors, as well as to streamline the operation of the model. Quite significantly, the model results are consistent with results from previous studies, including higher-resolution LES.

We have several improvements to add to the model in the near future. The addition of a temperature inversion will cap the circulations more realistically than will use of a rigid lid upper boundary condition (Lauferweiler and Shirer 1995). We have a separate routine ready to be tested, that will calculate the mean-wind profile parameters d_u and d_v needed to approximate other known profiles, such as an Ekman profile, with profiles obeying our boundary conditions. We will use these profiles to help us compare our preferred aspect ratio and orientation results with those obtained from stress-free models. We also plan to calculate the sub-BLSE fluxes, which may help us to better understand the heat and momentum flux profiles given by our model. The current results are very promising and show that the model is now ready to be used in further studies of how BLSE affect the sea-surface stress variability in different boundary layer configurations.

REFERENCES

- Alpers, W. and B. Brümmer, 1994: Atmospheric boundary layer rolls observed by the synthetic aperture radar: a review. *Rev. Geophys. Space Phys.*, **99**, 12613-12621.
- Brown, R. A., 1980: Longitudinal instabilities and secondary flows in the planetary boundary layer: A review. *Rev. Geophys. Space Phys.*, **18**, 683-697.
- Brümmer, B. and B. Busack, 1990: Convective patterns within a field of stratocumulus. *Mon. Wea. Rev.*, **118**, 801-817.
- Deardorff, J. W., 1976: Discussion of "thermals over the sea and gull flight behavior". *Bound. Lay. Meteo.*, 241-246.
- Etling, D. and R. A. Brown, 1993: Roll vortices in the planetary boundary layer: A review. *Bound. Lay. Meteo.*, **65** 215-248.
- Gerling, T. W., 1985: Remote sensing of the ocean-surface wind field with a scatterometer and a synthetic aperture radar. *John Hopkins APL Digest*, **6**, 320-329.
- Gerling, T. W., 1986: Structure of the surface wind field from the Seasat SAR. *J. Geophys. Res.*, **91**, 2308-2320.
- Haack, T. and H. N. Shirer, 1992: Mixed convective-dynamic roll vortices and their effects on initial wind and temperature profiles. *J. Atmos. Sci.*, **49**, 1181-1201.
- Higgins, R. W., 1987: From the equations of motion to spectral models. *Nonlinear Hydrodynamic Modeling: A Mathematical Introduction. Lecture Notes in Physics*, **271**, H. N. Shirer, Ed., Springer-Verlag, 47-69.
- Laufersweiler, M. J. and H. N. Shirer, 1989: A simple dynamical model of a stratocumulus-topped boundary layer. *J. Atmos. Sci.*, **46**, 1133-1153.
- Laufersweiler, M. J. and H. N. Shirer, 1995: A theoretical model of multiregime convection in a stratocumulus-topped boundary layer. *Bound. Lay. Meteo.*, **73**, 373-409.
- Lenschow, D. H. and P. L. Stephens, 1980: The role of thermals in the convective boundary layer. *Bound. Lay. Meteo.*, **19**, 509-532.

- Lenschow, D. H., J. C. Wyngaard, and W. T. Pennell, 1980: Mean field and second moment budgets in a baroclinic convective boundary layer. *J. Atmos. Sci.*, **37**, 1313-1326.
- Lilly, D. K., 1966: On the instability of Ekman boundary flow. *J. Atmos. Sci.*, **23**, 481-494.
- Pyle, R. J., 1987: Typical branching forms: Periodic solutions. *Nonlinear Hydrodynamic Modeling: A Mathematical Introduction. Lecture Notes in Physics*, **271**, H. N. Shির, Ed., Springer-Verlag, 264-291.
- Schmidt, H. and U. Schumann, 1989: Coherent structure of the convective boundary layer derived from large-eddy simulations. *J. Fluid Mech.*, **200**, 511-562.
- Shirer, H. N., 1986: On cloud street development in three dimensions: Parallel and Rayleigh instabilities. *Contrib. Atmos. Phys.*, **59**, 126-149.
- Shirer, H. N., Ed., 1987: *Nonlinear Hydrodynamic Modeling: A Mathematical Introduction. Lecture Notes in Physics*, **271**, Springer-Verlag, 546 pp.
- Sikora, T. D. and G. S. Young, 1993: Observations of planview flux patterns within convective structures of the marine atmospheric surface layer. *Bound. Lay. Meteo.*, **65** 273-288.
- Sikora, T. D., G. S. Young, R. C. Beal, and J. B. Edson, 1995: On the use of ERS-1 synthetic aperture radar images of the sea-surface in determining marine atmospheric boundary layer structure. To appear in *Mon. Wea. Rev.*
- Stensrud, D. J., 1987: The expected branching solution: Preferred wavelengths and orientations. *Nonlinear Hydrodynamic Modeling: A Mathematical Introduction. Lecture Notes in Physics*, **271**, H. N. Shirer, Ed., Springer-Verlag, 292-324.
- Stensrud, D. J. and H. N. Shirer, 1988: Development of boundary layer rolls from dynamic instabilities. *J. Atmos. Sci.*, **45**, 1007-1019.
- Stull, R. B., 1988: *An Introduction to Boundary Layer Meteorology*. Kluwer Academic Publishers, Boston, 666 pp.
- Vesecky, J. F. and R. H. Stewart, 1982: The observation of ocean surface phenomena using imagery from the SEASAT synthetic aperture radar: An assessment. *J. Geophys. Res.*, **87**, 3397-3430.

- Woodcock, A. H., 1940: Convection in the atmospheric boundary layer. *J. Marine Res.*, **3**, 248-253.
- Woodcock, A. H., 1975: Thermals over the sea and gull flight behavior. *Bound. Lay. Meteo.*, **9**, 63-68.
- Zuccarello, L. V., 1994: Modeling sea-surface stress variability caused by kilometer-scale marine atmospheric boundary layer circulations. MS Thesis, The Pennsylvania State University, 64pp.

Appendix A

MODEL ENERGETICS

We analyzed the energetics of the dimensionless model equations to identify all energy sources and sinks. This analysis was essential as a diagnostic tool. We compared the results from the original equation of motion and the vorticity equation used in the model, to determine the conditions ensuring that there were no new energy sources or sinks introduced by use of the vorticity equation.

We began the analysis by deriving the kinetic energy (KE) rate equation from the equation of motion. Using the available potential energy (AE) to KE conversion term in the KE rate equation to provide the definition for AE , we derived the AE rate equation from the thermodynamic equation. We derived another KE rate equation from the vorticity equation. We concluded the analysis by comparing the energy rate equations, justifying the energy sources and sinks, and identifying the boundary conditions needed to make both equations the same.

We derived the first KE rate equation by first multiplying the equation of motion by the velocity vector \mathbf{v}^* and then taking the volume integral of the product:

$$\int_v \left\{ \mathbf{v}^* \cdot \left[\frac{\partial \mathbf{v}^*}{\partial t^*} = -a_x \tilde{\nabla} p^* + P \tilde{\nabla}^2 \mathbf{v}^* - f^* P \mathbf{k} \times \mathbf{v}^* + P T^* \mathbf{k} \right. \right. \\ \left. \left. - (\text{Re} \mathbf{V}^* + \mathbf{v}^*) \cdot \tilde{\nabla} \mathbf{v}^* - \text{Re} w^* \frac{\partial \mathbf{V}^*}{\partial z^*} \right] \right\} dV, \quad (\text{A.1})$$

where

$$\tilde{\nabla} = a_x \frac{\partial}{\partial x^*} \mathbf{i} + a_y \frac{\partial}{\partial y^*} \mathbf{j} + \frac{\partial}{\partial z^*} \mathbf{k} = a_k \delta_{ki} \frac{\partial}{\partial x_i^*} \hat{\mathbf{x}}_i. \quad (\text{A.2})$$

The horizontal aspect ratios are $a_1 = a_x$ and $a_2 = a_y$; we set $a_3 = a_z = 1$. In the equations below, we use the notation in the last term in (A.2).

We rewrite the first term so that the time derivative is outside the volume integral. The result is a time derivative of KE , denoted \dot{KE} , as follows:

$$\int_V \mathbf{v}^* \cdot \frac{\partial \mathbf{v}^*}{\partial t^*} dV = \frac{\partial}{\partial t^*} \int_V \left(\frac{\mathbf{v}^* \cdot \mathbf{v}^*}{2} \right) dV = \frac{\partial}{\partial t^*} \int_V \left(\frac{v_i^{*2}}{2} \right) dV = \frac{\partial KE}{\partial t^*} = \dot{KE}. \quad (\text{A.3})$$

The result of calculating the vector dot product of the right side of the equation, using integration by parts, introducing the boundary conditions (2.34) - (2.39), and integrating over z^* when possible, is:

$$\begin{aligned} \dot{KE} = & \int_B -a_x w^* p^* \Big|_{z^*=0} dB - \int_V P \left(a_k \delta_{ki} \frac{\partial v_j^*}{\partial x_i} \right)^2 dV - \int_B P \left(\frac{u^{*2}}{s_m} + \frac{v^{*2}}{s_m} + w^* \frac{\partial w^*}{\partial z^*} \right) \Big|_{z^*=0} dB \\ & (1) \qquad (2) \qquad (3) \\ & + \int_V PT^* w^* dV + \int_B \frac{w^* v_i^{*2}}{2} \Big|_{z^*=0} dB - \int_V \text{Re} w^* v_i^* \frac{\partial V_i^*}{\partial z^*} dV, \quad (\text{A.4}) \\ & (4) \qquad (5) \qquad (6) \end{aligned}$$

where B is the horizontal boundary and we use the definition of $\tilde{\nabla}$ in (A.2).

The six terms on the right side of (A.4) represent sources and sinks of energy. The first term is a boundary term due to pressure work. The second term is traditionally the KE dissipation term and is clearly an energy sink. The third and fifth terms are also boundary terms. The three boundary terms (1), (3), and (5) are either energy sources or sinks depending on the sign of the velocity term within the integral and the sign of the

velocity Schramm constant, s_m in term (3) (for this model $s_m > 0$). The fourth term is a convective energy source term describing the conversion of AE to KE . We denote it as $C(AE, KE)$. The last term (6) is a KE generation or Reynolds stress term representing the dynamic source of energy.

We used the $C(AE, KE)$ term in (A.4), $C(AE, KE) = \int PT^* w^* dV$, to derive the AE rate equation, denoted \dot{AE} . We need the same term, but with the opposite sign, in the AE rate equation. We derived the \dot{AE} equation by multiplying the volume integral of the thermodynamic equation by an appropriate factor to obtain $-C(AE, KE)$. At first, we determined this factor to be $-PT^* / Ra$:

$$\int_V \left\{ \left[\frac{\partial T^*}{\partial t^*} = \tilde{\nabla}^2 T^* - Re \mathbf{V}^* \cdot \tilde{\nabla} T^* + Ra w^* - \mathbf{v}^* \cdot \tilde{\nabla} T^* \right] * \left(-\frac{PT^*}{Ra} \right) \right\} dV. \quad (A.5)$$

However, looking at the first term, we see that

$$\frac{\partial}{\partial t^*} \int_V \left(-\frac{PT^{*2}}{2Ra} \right) dV = \dot{AE}. \quad (A.6)$$

This term is valid only for the case $Ra < 0$, since AE must be nonnegative.

In our model we want the value of Ra to be unrestricted and so we introduce a correction term by adding and subtracting the vertical velocity, $-w^* + w^*$, to the thermodynamic equation. We then multiply the thermodynamic equation by PT^* to obtain:

$$\int_V \left\{ \left[\frac{\partial T^*}{\partial t^*} = \tilde{\nabla}^2 T^* - Re \mathbf{V}^* \cdot \tilde{\nabla} T^* + Ra w^* - w^* + w^* - \mathbf{v}^* \cdot \tilde{\nabla} T^* \right] * (PT^*) \right\} dV. \quad (A.7)$$

We now get an \dot{AE} definition that holds for any value of Ra :

$$\frac{\partial}{\partial t^*} \int_V \left(\frac{PT^{*2}}{2} \right) dV = \dot{AE}. \quad (\text{A.8})$$

After integrating by parts, applying the boundary conditions (2.34) - (2.39), and integrating over z^* when possible, we get the \dot{AE} equation:

$$\begin{aligned} \dot{AE} = & \int_B \frac{T^{*2}}{s_T} \Big|_{z^*=0} dB - \int_V P \left| a_i \frac{\partial T^*}{\partial x_i^*} \right|^2 dV + \int_V (Ra + 1) PT^* w^* dV \\ & (1) \qquad \qquad \qquad (2) \qquad \qquad \qquad (3) \\ & - \int_V PT^* w^* dV + \int_B \frac{PT^{*2} w^*}{2} \Big|_{z^*=0} dB. \end{aligned} \quad (\text{A.9})$$

(4) \qquad \qquad \qquad (5)

The six terms on the right side of (A.9) represent sources and sinks of AE . The first term is a boundary term that depends on the sign of the temperature Schramm constant, s_T . We use $s_T > 0$ in this model, so the term (1) is an AE source. The second term is an AE dissipation term and is clearly a sink. The third term comes from the original Rayleigh term in the thermodynamic equation and our correction term. This term is an AE source for $Ra > -1$ and a sink for $Ra < -1$. The case of $Ra = -1$ corresponds to a thermodynamically neutral atmosphere. In term (4), we find the $C(AE, KE)$ term of the \dot{KE} equation, but with the opposite sign. It represents a source or sink of AE , but not a net source of total energy $KE + AE$. The last term is another boundary term, and, depending on the sign of the vertical velocity at $z^* = 0$, is either a source or sink of AE .

We completed the energetics analysis for the original equations of the problem based on our original boundary conditions. Now we need to analyze the vorticity equation used in the model. For physical consistency, we must obtain the same \dot{KE} equation found from the equation of motion (A.3). To get this form, we recognize that the velocity perturbation in the model (Zuccarello, 1994) is $\mathbf{v}^* = \tilde{\nabla} \times \mathbf{A}^*$, where the vector streamfunction \mathbf{A}^* is the sum of the two vector streamfunctions ψ^* and η^* :

$$\mathbf{v}^* = \tilde{\nabla} \times \mathbf{A}^* = \tilde{\nabla} \times \psi^* + \tilde{\nabla} \times \eta^*. \quad (\text{A.10})$$

We then use a vector identity and rearrange its terms to give:

$$\mathbf{A}^* \cdot (\tilde{\nabla} \times \mathbf{v}^*) = \tilde{\nabla} \cdot (\mathbf{v}^* \times \mathbf{A}^*) + \mathbf{v}^* \cdot (\tilde{\nabla} \times \mathbf{A}^*). \quad (\text{A.11})$$

We then substitute $\mathbf{v}^* = \tilde{\nabla} \times \mathbf{A}^*$ into the last term to obtain:

$$\mathbf{A}^* \cdot (\tilde{\nabla} \times \mathbf{v}^*) = \tilde{\nabla} \cdot (\mathbf{v}^* \times \mathbf{A}^*) + \mathbf{v}^* \cdot \mathbf{v}^*. \quad (\text{A.12})$$

So, by vector multiplying the vorticity equation by the vector streamfunction \mathbf{A} , we get the dot product of the velocity vector needed to form \dot{KE} , together with another term.

We multiply the vorticity equation by \mathbf{A} and integrate the product over the volume V :

$$\int_V \left\{ \mathbf{A}^* \cdot \left[\frac{\partial (\tilde{\nabla} \times \mathbf{v}^*)}{\partial t^*} = P \tilde{\nabla}^2 (\tilde{\nabla} \times \mathbf{v}^*) - f^* P (\tilde{\nabla} \times (\mathbf{k} \times \mathbf{v}^*)) + P (\tilde{\nabla} \times T^* \mathbf{k}) \right. \right. \\ \left. \left. - \text{Re} \tilde{\nabla} \times (\mathbf{V}^* \cdot \tilde{\nabla} \mathbf{v}^*) - \text{Re} \tilde{\nabla} \times \left(w^* \frac{\partial \mathbf{V}^*}{\partial z^*} \right) - \tilde{\nabla} \times (\mathbf{v}^* \cdot \tilde{\nabla} \mathbf{v}^*) \right] \right\} dV. \quad (\text{A.13})$$

The result, after vector multiplication, integration by parts, application of (A.10), (A.12) and the boundary conditions (2.34) - (2.39), and integration over z^* when possible, is:

$$\dot{KE} = - \int_V P \left(a_k \delta_{ki} \frac{\partial v_j^*}{\partial x_i} \right)^2 dV - \int_B P \left(\frac{u^{*2}}{s_m} + \frac{v^{*2}}{s_m} + w^* \frac{\partial w^*}{\partial z^*} \right) \Big|_{z^*=0} dB \quad (2)$$

$$+ \int_V PT^* w^* dV + \int_B \frac{w^* v_i^{*2}}{2} \Big|_{z^*=0} dB - \int_V \text{Re} w^* v_i^* \frac{\partial V_i^*}{\partial z^*} dV \quad (3)$$

$$+ \int_B A_i \frac{\partial}{\partial t^*} \frac{\partial A_i}{\partial z^*} \Big|_{z^*=0} dB - \int_B P A_i a_k^2 \delta_{kj} \frac{\partial^2}{\partial x_j^{*2}} \frac{\partial A_i}{\partial z^*} \Big|_{z^*=0} dB + \int_B \varepsilon_{3jk} f^* P A_k \frac{\partial A_j}{\partial z^*} \Big|_{z^*=0} dB \quad (4)$$

$$+ \int_B \text{Re} A_i V_j^* a_k \delta_{kj} \frac{\partial}{\partial x_j^*} \frac{\partial A_i}{\partial z^*} \Big|_{z^*=0} dB - \int_B \varepsilon_{i3j} \text{Re} A_i w^* \frac{\partial V_j^*}{\partial z^*} \Big|_{z^*=0} dA \quad (5)$$

$$+ \int_B \varepsilon_{ijk} A_i a_m \delta_{mj} \frac{\partial A_k}{\partial x_j^*} a_n \delta_{ni} \frac{\partial}{\partial x_i^*} \frac{\partial A_l}{\partial z^*} \Big|_{z^*=0} dB, \quad (A.14)$$

(12)

where the tensor A_k is the streamfunction component ψ^* when $k = 1$, η^* when $k = 2$, and 0 when $k = 3$.

Now, we compare the two \dot{KE} equations (A.4) and (A.14). We do not find term (1), the pressure boundary term in (A.4), directly in (A.14). However, we find the next five terms in both (A.4) and (A.14). The terms are: the dissipation term (2); a boundary term (3); the $C(AE, KE)$ term (4); another boundary term (5); and the KE generation term (6). We can find no direct comparison in (A.4) with the six remaining terms in (A.14).

Therefore, these six terms must come from the pressure boundary term in (A.4), since these two equations must be equal and the pressure boundary term is the only term not found in (A.14).

It would be much easier to study the energetics of the model if we could eliminate the unwanted sources and sinks of energy. In both \dot{KE} equations and the \dot{AE} equation, the unwanted sources and sinks are boundary integrals with $w^*(z^* = 0)$ and $A_i(z^* = 0)$ in them. By making $w^*(z^* = 0) = 0$ and $A_i(z^* = 0) = 0$, as explained in Appendix B, we make these boundary terms vanish. (Note that we assume $\partial w^*/\partial z^*$ is finite at $z^* = 0$, which is a realistic condition.) With these boundary conditions, the energy rate equations (A.4) = (A.14) and (A.9) become:

$$\begin{aligned} \dot{KE} = & - \int_V P \left(a_k \delta_{ki} \frac{\partial v_j^*}{\partial x_i} \right)^2 dV - \int_B P \left(\frac{u^{*2}}{s_m} + \frac{v^{*2}}{s_m} \right) \Big|_{z^*=0} dB + \int_V P T^* w^* dV \\ & (1) \qquad (2) \qquad (3) \end{aligned}$$

$$- \int_V \text{Re} w^* v_i^* \frac{\partial V_i^*}{\partial z^*} dV \quad (\text{A.15})$$

$$\begin{aligned} \dot{AE} = & \int_B \frac{T^{*2}}{s_T} \Big|_{z^*=0} dB - \int_V P \left(a_k \delta_{ki} \frac{\partial T^*}{\partial x_i} \right)^2 dV + \int_V (Ra + 1) P T^* w^* dV - \int_V P T^* w^* dV. \quad (\text{A.16}) \\ & (1) \qquad (2) \qquad (3) \qquad (4) \end{aligned}$$

We have rectified the model energetics. In the \dot{KE} equation the terms are: KE dissipation (1), a boundary KE sink term (2) (since $s_m > 0$), the $C(AE, KE)$ term (3), and the KE generation term (4). Similar terms are in the \dot{AE} equation: a boundary AE source term (1) (since $s_T > 0$), the AE dissipation term (2), the AE generation term (3), and the $C(AE, KE)$ term (4). Note that for $Ra = -1$, the boundary layer flow is driven only by heat

flux from the bottom and modified only by shear. We examine this special case in this thesis.

Appendix B

MODIFICATION OF THE VERTICAL BASIS FUNCTION

The energetics analysis, discussed in Appendix A, resulted in boundary conditions $\mathbf{A}^*(z^* = 0) = 0$, which imply $w^*(z^* = 0) = 0$, that supplement the original Monin-Obukhov boundary conditions (2.34) - (2.39). After discovering the need for these new vertical boundary conditions, we did not want to completely rederive the model. Therefore, we reformulated the vertical velocity basis functions to satisfy both the new and the old boundary conditions, and then we changed the program to account for these changes. This appendix explains the vertical basis function reformulation and the modifications to the existing program.

B.1. Vertical Basis Function Reformulation

We start by looking at the condition $\mathbf{A}^*(0) = 0$, and then extending it to the condition $w^*(0) = 0$. We represent the velocity vector \mathbf{v}^* as the curl of a vector streamfunction \mathbf{A}^* , which is the sum of two vector streamfunctions ψ^* and η^* . Therefore, we may express the velocity perturbation \mathbf{v}^* as

$$\mathbf{v}^* = \tilde{\nabla} \times \mathbf{A}^* = \tilde{\nabla} \times \psi^* + \tilde{\nabla} \times \eta^*. \quad (\text{B.1})$$

We use a truncated Fourier expansion to represent the dependent vector streamfunctions ψ^* and η^* . Accordingly, the vector streamfunction \mathbf{A}^* is

$$\mathbf{A}^*(x^*, y^*, z^*, t^*) = \sum_{p=0}^4 \sum_{q=1}^4 \left[\left\{ \psi_{pq}(t^*) \text{trig}_p(x^*, y^*) h_q(z^*) \right\} \mathbf{i} + \left\{ \eta_{pq}(t^*) \text{trig}_p(x^*, y^*) h_q(z^*) \right\} \mathbf{j} + 0 \mathbf{k} \right], \quad (\text{B.2})$$

where the only dependence on z^* is in the vertical basis function, $h_q(z^*)$. If we want $\mathbf{A}^*(z^* = 0) = 0$, then we must force $h_q(0) = 0$, for each of the vertical wavenumbers, q .

The vertical basis function is

$$h_q(z^*) = \cos \varpi_q z^* - s_m \varpi_q \sin \varpi_q z^* \text{ for } q = 1, 2, 3, 4, \quad (\text{B.3})$$

where $\varpi_1, \varpi_2, \varpi_3, \varpi_4$ are the first four positive solutions of

$$s_m \varpi_q = \cot \varpi_q. \quad (\text{B.4})$$

The vertical basis function values at the vertical boundaries are:

$$h_q(1) = 0 \quad (\text{B.5})$$

$$h_q(0) = 1. \quad (\text{B.6})$$

Using (B.6), we find a very simple way to make the new vertical basis functions vanish that leads to $\mathbf{A}^*(z^* = 0) = 0$. We define new vertical basis functions $h_{\text{new}q'}$, for

$q' = 1, 2, 3$, by taking appropriate differences of the old basis functions $h_{\text{old}q} = h_q$:

$$h_{new1} = h_{old1} - h_{old2} \quad (B.7)$$

$$h_{new2} = h_{old2} - h_{old3} \quad (B.8)$$

$$h_{new3} = h_{old3} - h_{old4}. \quad (B.9)$$

The three new vertical basis functions reduce the number of vertical wavenumbers in the vorticity representation from four to three. We use (B.3) to define the old basis functions and then use these to obtain the new basis functions (B.7) - (B.9). We use these new functions to plot the vertical velocity profiles, as shown in Fig. B.1.

Once put into a new Galerkin expansion, the resulting new function satisfies the boundary condition $\mathbf{A}^*(z^* = 0) = 0$:

$$\begin{aligned} \mathbf{A}^*(x^*, y^*, z^*, t^*) = \sum_{p=0}^4 \sum_{q'=1}^3 \left[\left\{ \psi_{pq'}(t^*) \text{trig}_p(x^*, y^*) h_{newq'}(z^*) \right\} \mathbf{i} \right. \\ \left. + \left\{ \eta_{pq'}(t^*) \text{trig}_p(x^*, y^*) h_{newq'}(z^*) \right\} \mathbf{j} + 0\mathbf{k} \right]. \end{aligned} \quad (B.10)$$

Substituting (B.7)-(B.9) in (B.10) yields

$$\begin{aligned} \mathbf{A}^*(x^*, y^*, z^*, t^*) = \sum_{p=0}^4 \sum_{q'=1}^3 \left[\left\{ \psi_{pq'}(t^*) \text{trig}_p(x^*, y^*) (h_{oldq'}(z^*) - h_{oldq'+1}(z^*)) \right\} \mathbf{i} \right. \\ \left. + \left\{ \eta_{pq'}(t^*) \text{trig}_p(x^*, y^*) (h_{oldq'}(z^*) - h_{oldq'+1}(z^*)) \right\} \mathbf{j} + 0\mathbf{k} \right]. \end{aligned} \quad (B.11)$$

At $z^* = 0$, the old basis functions $h_{oldq} = 1$ by (B.6) and therefore their differences in (B.11) cancel. Summing over p and q' results in $\mathbf{A}^*(z^* = 0) = 0$.

When we carry out the curl of \mathbf{A}^* in (B.11), we get the new velocity component equations. The vertical velocity equation is:

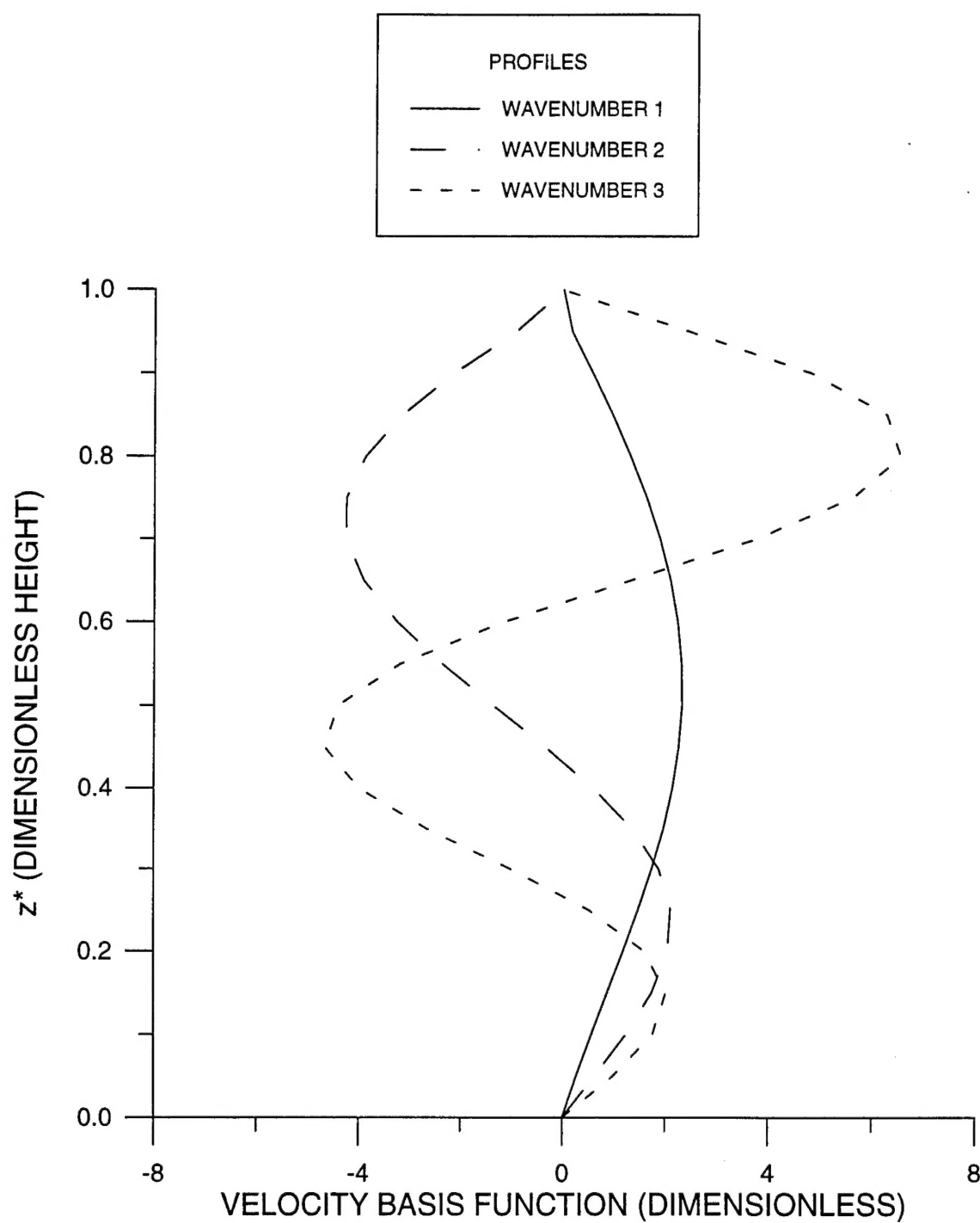


Fig. B.1. Velocity vertical basis function (vertical velocity) profiles (B.7) - (B.9) for the three new wavenumbers.

$$w^*(x^*, y^*, z^*, t^*) = \sum_{p=0}^4 \sum_{q'=1}^3 \left[\eta_{pq'}(t^*) \frac{\partial}{\partial x} \text{trig}_p(x^*, y^*) h_{newq'}(z^*) - \psi_{pq'}(t^*) \frac{\partial}{\partial y} \text{trig}_p(x^*, y^*) h_{newq'}(z^*) \right]. \quad (\text{B.12})$$

Summing over p and q' , we get $w^*(0) = 0$, which is our other new boundary condition.

This accomplishes our first goal of making $w^*(0) = 0$ and $A^*(0) = 0$.

B.2. Modification of Existing Program to Incorporate New Basis Functions

To account for the new boundary conditions, we adjust the existing model by rewriting the portions of the code involving the vertical velocity basis function h_q . When we define the new vertical basis function $h_{newq'}$, we reduce the streamfunction vertical wavenumbers from four to three. This result reduces the number of model equations and coefficients from 60 to 50. We now integrate the model with a 50-element amplitude coefficient vector y . Therefore, as for the 60 coefficient models, we construct each of the matrices: the temporal derivative matrix A , the linear matrix B , and the y -dependent nonlinear matrix C , as 50×50 matrices.

$$A\dot{y} = By + C(y)y, \quad (\text{B.13})$$

In the linear portion of the program, we introduce the new vertical basis function definitions (B.7) - (B.9) into the appropriate integrals. This process is straightforward and produces the 50×50 matrices A and B . It is a little more complicated for the y -dependent nonlinear matrix C . Zuccarello (1994) derives the nonlinear portion of the model using DERIVE to find the integrals of the products of the vertical basis functions.

He defines these integrals using two- and three-dimensional arrays in the nonlinear subroutine. To avoid rederiving with (B.7) - (B.9), the equations used to define the arrays for C , we found we could index and appropriately difference these arrays to get the new integral, that are composed of the products of the new vertical basis functions h_{newq} . The result is a 50×50 matrix C . Thus the model is strictly a 50 coefficient system, and is integrated numerically as such.